Ludwig Maximilian Universität - München

Sektion Physik

Feasibility Study of a Magnetic Monopole Trigger in $p\bar{p}$-collisions

Philipp Schieferdecker

Diplomarbeit - Diploma Thesis

1. August 2001

Erstgutachterin: Prof. Dr. Dorothee Schaile,
Zweitgutachter: Prof. Dr. Christian Kiesling

Contents

List of Figures

List of Tables

Chapter 1

Introduction

In 1909, Robert A. Milikan discovered the quantization of electric charge by carrying out his famous oil drop experiment. Ever since, though of fundamental importance for all of today's physical descriptions of nature, this quantization remains mysterious; its explanation is one of nature's best kept secrets. In 1931, Paul A.M. Dirac, known for his affinity to mathematical beauty, proved not just the consistency of magnetic monopoles with electrodynamics but also, how the existence of both electric and magnetic charge requires charge quantization [1]. This Dirac Quantization Condition (DQC) and the elegant symmetry implied for electrodynamics keep physicists searching for magnetic charge. Moreover, no theoretical principle or experimental evidence contradicts their existence.

Monopole searches have been carried out with both high energy and cosmic ray detectors. While the later seek to detect magnetic charge produced by the universe, high energy particle accelerators investigate their direct production in $p\bar{p}$ and in e^+e^- collisions. Indirect searches have been carried out considering particle interactions which involve virtual monopoles. They depend on a sound theoretical understanding in order to interpret the results.

Experiments at the MACRO detector at LNGS in Gran Sasso (Italy) [2] searched for super heavy (10^{16} TeV/c^2) monopoles predicted by GUT theories in penetrating cosmic radiation. Independent analyses were carried out with the scintillator, streamer tubes and nuclear track subdetectors, making use of the highly ionizing signature of magnetic charge. No candidates were found in several years of data taking. Since Dirac's theory does not motivate these

monopoles and a typical $p\bar{p}$ beam can not produce them, GUT monopoles are not considered here.

The D0 Collaboration investigated a process involving photon-photon scattering through a virtual magnetic monopole loop [3]. A previous study by the L3 experiment at the LEP e^+e^- collider searched for the $Z \rightarrow \gamma\gamma\gamma$ decay through a similar virtual monopole loop diagram [4]. Indirect approaches make predictions on monopole masses far beyond the center of mass energy of the respective beams, but the results are uncertain. Numerous attempts have failed to produce a QED theory containing monopoles that adequately describes their production. The enormous coupling of magnetic charge implied by the DQC makes any perturbative approach useless. Although the the alternative, developing a non-perturbative dual QED, is a great challenge, promising efforts have been made in this direction [6]. Results on monopole production are expected soon. However, both indirect searches are based on cross section calculations which violate perturbative requirements; it has been argued, that no valid results can be derived this way [5]. Note that the presented limits of the order of 1 TeV would make direct production and discovery at current beam energies impossible.

A group at the University of Oklahoma is currently performing a direct monopole search, looking for low mass Dirac monopoles bound and trapped in detector material exposed to the Tevatron beam in Run I of the D0 experiment [8]. This approach is dependent on the model how magnetic charge is trapped in matter. The production mechanism used in what follows is very similar to the one presented by the Oklahoma group; it assumes a Drell-Yan like monopole pair production. The same theorists who are currently developing a non-perturbative dual QED consider this the best one can do in the absence of a sound field theory [5]. The obtained lower limit for monopole masses is 285 GeV; a direct search in Run II can reach monopole masses up to 550 GeV. This opens a window for monopole discovery in the upcoming data taking period of the Tevatron collider.

This study evaluates a direct search for magnetic charge in Run II of the CDF experiment using the newly installed Time-of-Flight system and a special Level-1 trigger sensitive to the highly ionizing signature of magnetic monopoles. The mass reach for a monopole discovery at CDF in Run II is investigated and the strategy of the Highly Ionizing Particle (HIP) trigger

is presented. To aid future Monte Carlo studies, the knowledge derived from stand alone monopole simulation has been implemented in GEANT[9]. Therefore, the presented results not only give insight on the possible performance of CDF in a direct search but also motivate and assist further studies of magnetic monopoles.

Chapter 2

Magnetic Monopoles and Electrodynamics

2.1 Symmetrized Maxwell Equations

The Maxwell Equations,

$$\vec{\nabla} \cdot \vec{D} = 4\pi\rho \tag{2.1}$$

$$\vec{\nabla} \cdot \vec{B} = 0 \tag{2.2}$$

$$-\vec{\nabla} \times \vec{E} = \frac{1}{c}\frac{\partial}{\partial t}\vec{B} \tag{2.3}$$

$$\vec{\nabla} \times \vec{H} = \frac{1}{c}\frac{\partial}{\partial t}\vec{D} + \frac{4\pi}{c}\vec{j} \tag{2.4}$$

represent a complete description of all known classical electromagnetic phenomena. Together with the Lorentz force law,

$$\vec{F} = e \cdot \left(\vec{E} + \frac{1}{c}\vec{v} \times \vec{B}\right)$$

and the Newton equations of motion they describe all classical dynamics of interacting charged particles and electromagnetic fields. Therefore, if one revises these equations in order to introduce magnetic charge, those modifications cannot change the electrodynamic description of the monopole-free nature that is already observed and understood.

In analogy to electrostatics, magnetic charge is added by introducing a magnetic charge density,

$$\vec{\nabla} \cdot \vec{B} = 4\pi\rho_m \ , \tag{2.5}$$

where indices m and e label electric and magnetic quantities. Now that magnetic fields are no longer due solely to the motion of an electric charge, Equation (2.3) has to be reevaluated. The co-moving time derivate of the magnetic field becomes

$$0 = \frac{d}{dt}\vec{B} = \frac{\partial}{\partial t}\vec{B} + \left(\vec{v} \cdot \vec{\nabla}\right) \vec{B} \tag{2.6}$$

and using the vector identity

$$\vec{\nabla} \times \left(\vec{a} \times \vec{b}\right) = \vec{a}\left(\vec{\nabla} \cdot \vec{b}\right) - \left(\vec{a} \cdot \vec{\nabla}\right)\vec{b}$$

it can be written as

$$-\vec{\nabla} \times \left(\vec{v} \times \vec{B}\right) = \frac{\partial}{\partial t}\vec{B} + \vec{v}\left(\vec{\nabla} \cdot \vec{B}\right).$$

Now we define the magnetic current density as $\vec{j}_m \equiv \rho_m \vec{v}$ and use Equation (2.5) to derive

$$\vec{v}\left(\vec{\nabla} \cdot \vec{B}\right) = 4\pi\vec{j}_m.$$

Recall that the Maxwell Equations imply

$$\vec{\nabla} \times \vec{E} = -\vec{\nabla} \times \left(\frac{\vec{v}}{c} \times \vec{B}\right)$$

which ensures that an electric charge with $|\vec{v}| = 0$ can induce an electric field. Finally, the complete set of *Symmetrized Maxwell Equations* reads as

$$\vec{\nabla} \cdot \vec{D} = 4\pi\rho_e \tag{2.7}$$

$$\vec{\nabla} \cdot \vec{B} = 4\pi\rho_m \tag{2.8}$$

$$-\vec{\nabla} \times \vec{E} = \frac{1}{c}\frac{\partial}{\partial t}\vec{B} + \frac{4\pi}{c}\vec{j}_m \tag{2.9}$$

$$\vec{\nabla} \times \vec{H} = \frac{1}{c}\frac{\partial}{\partial t}\vec{D} + \frac{4\pi}{c}\vec{j}_e \tag{2.10}$$

These modifications of the Maxwell Equations do not necessarily imply any physics beyond ordinary electrodynamics, because the Symmetrized Maxwell Equations are invariant under a duality transformation ($\xi \in \mathbb{R}$),

$$\begin{aligned}
\vec{E} &= \vec{E}' \cos\ \xi + \vec{H}' \sin\ \xi & \vec{D} &= \vec{D}' \cos\ \xi + \vec{B}' \sin\ \xi \\
\vec{H} &= -\vec{E}' \sin\ \xi + \vec{H}' \cos\ \xi & \vec{B} &= -\vec{D}' \sin\ \xi + \vec{B}' \cos\ \xi \\
\rho_e &= \rho_e' \cos\ \xi + \rho_m' \sin\ \xi & \vec{j}_e &= \vec{j}_e' \cos\ \xi + \vec{j}_m' \sin\ \xi \\
\rho_m &= -\rho_e' \sin\ \xi + \rho_m' \cos\ \xi & \vec{j}_m &= -\vec{j}_e' \sin\ \xi + \vec{j}_m' \cos\ \xi\ .
\end{aligned}$$

Evidently, the original Maxwell Equations are one representation for one special angle ξ motivated by the experimental evidence of the absence of magnetic charge. Any other representation describes electrodynamics just as well even though it would assign every known charged particles a magnetic charge, but deal with a different set of fields at the same time. For any given ξ, the ratio between electric and magnetic charge for any known single electrically charged particle would be the same. Therefore, the existence of magnetic charges ultimately comes down to the question, if any particle exists, which has a ratio of electric and magnetic charge different to "purely" electrically charged particles for every given ξ.

Taking $\xi = \pi/2$, the Symmetrized Maxwell Equations are invariant under the transformation

$$\begin{aligned}
&\rho_e \to \rho_m & &\vec{j}_e \to \vec{j}_m & &\vec{E} \to \vec{H} & &\vec{D} \to \vec{B} \\
&\rho_m \to -\rho_e & &\vec{j}_m \to -\vec{j}_e & &\vec{B} \to -\vec{D} & &\vec{H} \to -\vec{E}\ ,
\end{aligned} \tag{2.11}$$

which switches electric and magnetic quantities. This symmetry suggests a generalized Lorentz force for a particle with electric charge e and magnetic charge g:

$$\vec{F} = e\left(\vec{E} + \frac{\vec{v}}{c} \times \vec{B}\right) + g\left(\vec{B} - \frac{\vec{v}}{c} \times \vec{E}\right)\ . \tag{2.12}$$

The symmetries of ρ_m under both spatial inversion and time reversal are opposite of those of ρ_e. As a consequence, if dyons, particles with both electric and magnetic charge, exist then space inversion and time reversal would no longer be valid symmetries.

2.2 Monopole motion in a constant magnetic field

Since the CDF II detector like many other tracking systems features a constant magnetic field along the beam axis,

$$\vec{B} = B \cdot \vec{e}_z$$

the trajectory of a particle carrying a magnetic charge only will be derived for this configuration. All calculations will be performed in natural units. According to Equation (2.12), the monopole accelerates along the beam (z-axis) but maintains constant ϕ. Therefore, it will remain in the plane determined by its initial direction and the problem is reduced to two dimensions. The axis parallel to the monopole's initial transverse momentum will be indexed "t" throughout this section with unit vector $\vec{e}_t$.

Consider the special case of a particle starting out at the origin with initial momentum perpendicular to the magnetic field:

$$\vec{p}_0 \perp \vec{B} \quad \rightarrow \quad \vec{p}_0 = p_{t_0} \cdot \vec{e}_t$$

Since no transverse force acts on the monopole, its transverse momentum is conserved and constant for all times. To ensure consistent labeling with the general solution, initial momentum end energy are labeled transverse even though they do not have any longitudinal component. The equation of motion, $\vec{F} = \gamma g \vec{B}$ supplies two differential equations for p_z and p_t:

$$\frac{d\vec{p}}{dt} = g\vec{B} \quad \Rightarrow \quad \dot{p}_z = gB, \qquad \dot{p}_t = 0$$

Integration and $p_i = m\gamma(v)\beta_i,\ i = z, t$ produces

$$p_z = gBt \quad \Leftrightarrow \quad \gamma\beta_z = \frac{g}{m}Bt \tag{2.13}$$

$$p_t = p_{t_0} \quad \Leftrightarrow \quad \gamma\beta_t = \frac{p_{t_0}}{m} \tag{2.14}$$

The two equations are coupled since $\gamma = 1/\sqrt{1 - \beta_z^2 - \beta_t^2}$. Eliminating γ delivers a relation between β_t and β_z:

$$\beta_z = \frac{gBt}{p_{t_0}}\beta_t. \tag{2.15}$$

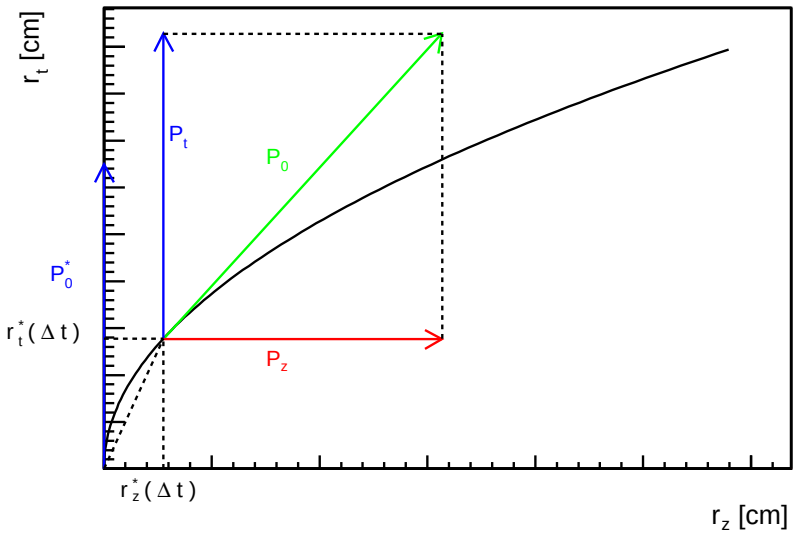

Figure 2.1: Trajectory of a monopole with initial momentum perpendicular to the magnetic field (black) and how trajectories with arbitrary initial momentum relate

Now they can be decoupled by squaring Equation (2.14)

$$\beta_t^2 = \left(\frac{p_{t_0}}{m}\right)\left(1 - \beta_t^2 - \beta_z^2\right)$$

and using Equation (2.15) to eliminate one velocity component:

$$\beta_z = \frac{gBt}{\sqrt{E_{t_0}^2 + (gBt)^2}} \qquad \beta_t = \frac{p_{t_0}}{\sqrt{E_{t_0}^2 + (gBt)^2}}$$

where $E_{t_0}^2 \equiv m^2 + p_{t_0}^2$ is the squared *total initial (transverse) energy*. Finally, integration in t delivers the trajectory $\vec{r}^{\star}(t) = (r_t^{\star}(t), r_z^{\star}(t))$ (the $\star$ indicates that it concerns the special solution with $\vec{p}_0 \parallel \vec{B}$):

$$\vec{r}^{\star}(t) = \left(\frac{p_{t_0}}{gB}\text{arsinh}\left(\frac{gBt}{E_{t_0}}\right)\right) \cdot \vec{e}_t + \left(\frac{\sqrt{E_{t_0}^2 + (gBt)^2} - E_{t_0}}{gB}\right) \cdot \vec{e}_z \tag{2.16}$$

Figure 2.1 shows such a monopole trajectory and illustrates how the general solution can be obtained from this special solution. Recall that since no force acts in the transverse direction, p_t is conserved. On the other hand, the time Δt after which the longitudinal momentum

component has been raised from zero to some value $p_z(\Delta t) \equiv p_{z_0}$ can be easily calculated according to Equation (2.13):

$$\Delta t = \frac{p_{z_0}}{F} = \frac{p_{z_0}}{gB}$$

Now the starting point $\vec{r}(t=0)$ of a monopole trajectory in the general case ($\vec{p_0} = (p_{t_0}, p_{z_0})$) is interpreted as the point $\vec{r}^*(t=\Delta t)$ on a special trajectory with $\vec{p_0} = (p_{t_0}, 0)$. Then the general solution can be derived by cutting away the part of the special solution resulting from times smaller than Δt:

$$\vec{r}(t) = \vec{r}^*(t+\Delta t) - \vec{r}^*(\Delta t) \tag{2.17}$$

The complete parameterization of a monopole track with arbitrary initial momentum in a constant magnetic field along the z-axis is therefore

$$\begin{aligned} \vec{r}(t) &= \frac{E_{t_0}}{gB}\left(\sqrt{1+\left(\frac{gB}{E_{t_0}}(t+\Delta t)\right)^2} - \sqrt{1+\left(\frac{gB}{E_{t_0}}\Delta t\right)^2}\right)\vec{e}_z + \\ &\quad \frac{p_{t_0}}{gB}\cdot\left(\operatorname{arsinh}\left(\frac{gB}{E_{t_0}}(t+\Delta t)\right) - \operatorname{arsinh}\left(\frac{gB}{E_{t_0}}\Delta t\right)\right)\vec{e}_t \end{aligned}$$

Note that E_{t_0} is still defined as the initial *transverse* energy and the initial longitudinal momentum component must not be included.

The track of a magnetic charge is a straight line in the $r-\phi$ plane and a parabola, stretched by relativistic effects, in the $r-z$ plane. This is a unique signature. it describes approximately a parabola in the longitudinal while moving on a straight line in the transversal plane. Further discussion and illustration will follow in Chapter 4.

2.3 Dirac Quantization Condition

P.A.M. Dirac discovered a quantization condition for electric and magnetic charge while dealing with the quantum mechanical treatment of an electron in the field of a monopole[1, 11]. A semiclassical illustration is presented to enlighten Dirac's idea of how the existence of magnetic monopoles forces charge quantization.

Consider the deflection of an electron by the field of a stationary monopole of magnetic charge g shown in Figure 2.2. For a very large impact parameter, the particle is approximately

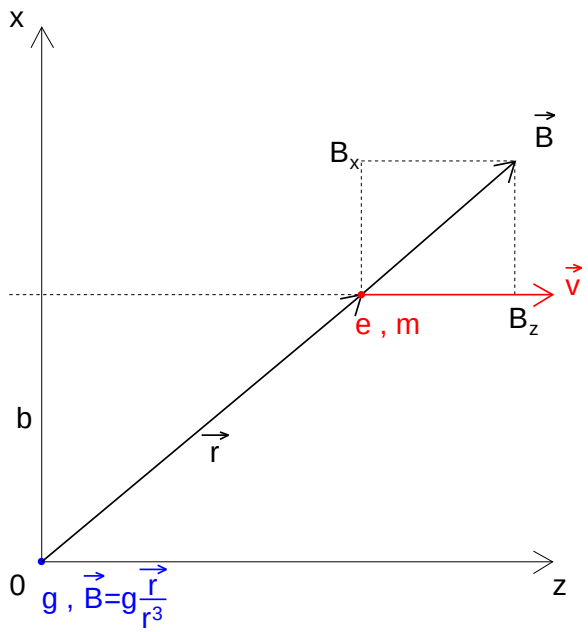

Figure 2.2: Electrically charged particle, crossing the field of a monopole with large impact parameter

undeflected, the trajectory is a straight line, and the change in angular momentum can be easily calculated. The magnetic field of the monopole is radially directed:

$$\vec{B} = g\frac{\vec{r}}{r^3}$$

Since the electron is undeflected, the only force acting throughout the collision points into the paper plane (y-axis):

$$F_y = e\beta B_x = \frac{eg}{c} \cdot \frac{vb}{\left(b^2 + v^2t^2\right)^{3/2}} \tag{2.18}$$

where b is the impact parameter. Now the impulse transmitted by this force can be calculated by time integration:

$$\Delta p_y = \int_{-\infty}^{\infty} F_y dt = \frac{2eg}{cb} \tag{2.19}$$

Therefore, the particle is deflected out of the paper in Figure 2.2 and its angular momentum, $\vec{L}$, has a non-zero z component after the collision:

$$\Delta L_z = r_x^f p_y^f - r_y^f p_x^f - \left(r_x^i p_y^i - r_y^i p_x^i\right) = r_x^f p_y^f = b\Delta p_y = \frac{2eg}{c} \tag{2.20}$$

where i (initial) and f (final) indicate the states before and after the collision respectively. Quantum mechanics demands, that any change in angular momentum must occur in integral multiples of $\hbar$, so the above quantity must be quantized:

$$\frac{ge}{\hbar c} = \frac{n}{2}, \quad n \in \mathbb{N} \tag{2.21}$$

Equation (2.21) is the *Dirac Quantization Condition* first published in 1931[1]. The existence of both electric and magnetic charge in the universe requires charge quantization. Since the quantization of the electric charge in nature is well established but still mysterious, the discovery of just a single monopole would provide a much wanted explanation.

2.4 Multiple Scattering and Energy Loss

A fast charged particle incident on matter makes collisions with the atomic electrons as well as with the nuclei of the medium. In case of particles much heavier than electrons, those two kinds of collisions have different consequences. If a heavy charged particle collides with an

atomic electron, the latter will absorb a considerable amount of the energy of the incoming particle while hardly deflecting it at all. A nucleus, being much heavier, will take up little energy but cause significant deflection due to its greater charge. These concepts lead to the two major effects on charged particles when passing matter: energy loss due to ionization and multiple scattering.

The energy loss due to ionization of a fast electrically charged particle can be calculated according to the *Bethe-Bloch-Formula*:

$$\frac{1}{\rho}\frac{dE}{dx} = D\frac{Z}{A}\frac{z^2}{\beta^2}\cdot\left(\ln\left(\frac{2m_e\beta^2\gamma^2T_{max}}{I^2}\right) - 2\beta^2 - \delta - \frac{2C_e}{Z}\right) \tag{2.22}$$

with

D	$2\pi N_A r_e^2 mc^2$	Z	*atomic number of medium*
A	*mass number of medium*	z	*charge of incident particle*
δ	*reduction term for density effect*	$\frac{C_e}{Z}$	*shell correction term*

and

$$T_{max} = \frac{2m_e\left(\gamma^2-1\right)}{1+2\gamma\frac{m_e}{M}+\left(\frac{m_e}{M}\right)^2} \tag{2.23}$$

the maximum energy transferable to the free electron. The density effect comes from the tendency of matter to become polarized as the incident particle velocity increases. The shell correction gains importance at low kinetic energies, especially in heavy elements, since the probability of collisions with electrons of inner atomic shells is small. Both effects will be neglected from now on unless explicitly noted. The energy loss due to ionization does not depend on the mass of the incident particle but just on its kinematic properties for $M \gg m_e$.

The deflection caused by atomic nuclei occurs many times during the passage of the incident particle through the medium. Many small angle scatters, which are mostly due to Coulomb scattering, cause the particle's total deflection. This process, refered to as multiple scattering, can be described by a Gaussian distribution for electrically charged particles and small deflection angles.

$$\theta_0 \equiv \theta_{plane}^{rms} \equiv \frac{1}{\sqrt{2}}\theta_{space}^{rms}$$

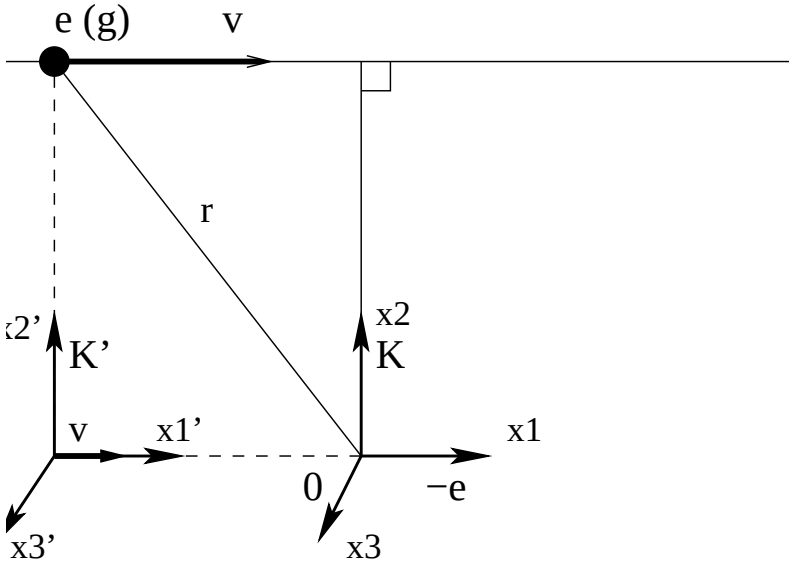

Figure 2.3: A relativistic electric (magnetic) charge passes an atomic electron, which rests at 0 in K

the width of this distribution of scattering angles is

$$\theta_0 = \frac{13.6 \text{ MeV}}{\beta cp} z \sqrt{\frac{x}{X_0}} \left(1 + 0.038 \ln\left(\frac{x}{X_0}\right)\right) \tag{2.24}$$

where z is the charge of the incident particle and x/X_0 is the thickness of the scattering medium in radiation lengths. Deflections into θ and ϕ are independent and equally distributed.

The formulas derived for electrically charged particles can be modified to sute magnetic charge through the substitution[5, 11, 12]

$$e \longrightarrow \beta \cdot n \cdot g \tag{2.25}$$

where g is the magnetic charge and n is the Dirac quantum number. The additional β factor is justified by comparing the energy transfer in a Coulomb collision between an atomic electron and electric or magnetic charge.

First consider an electrically charged particle colliding with an atomic electron in matter. The momentum transfer is assumed to be small and the particle therefore approximately undeflected. The atomic electron is considered to be at rest. The momentum impulse can be calculated from the electric field of the incident particle in the rest frame of the atomic electron. Applying a Lorentz transformation to the static field provides the electromagnetic

field components of the incident particle passing with velocity v at an impact parameter b as

$$E_1 = -\frac{e\gamma vt}{\left(b^2 + \gamma^2 v^2 t^2\right)^{3/2}} \tag{2.26}$$

$$E_2 = \frac{e\gamma b}{\left(b^2 + \gamma^2 v^2 t^2\right)^{3/2}} \tag{2.27}$$

$$B_3 = \beta E_2 \tag{2.28}$$

with the other components vanishing. Given that only E_2 has a non-vanishing time integral, the momentum impulse can be calculated as

$$\Delta p = \int_{-\infty}^{\infty} e \cdot E_2\left(t\right) dt = \frac{2e^2}{bc\beta} \tag{2.29}$$

and the the energy transfer to the electron is

$$\Delta E\left(b\right) = \frac{\left(\Delta p\right)^2}{2m} = \frac{2e^4}{mc^2\beta^2} \cdot \frac{1}{b^2} \ . \tag{2.30}$$

The corresponding field components to Equation (2.26) - Equation (2.28), where the incident particle is now a magnetic charge, can be obtained by applying the duality transformation 2.11:

$$e \to g \quad E \to B \quad B \to -E$$

Of the resulting components B_1, B_2, and E_3, only the electric field can do work on the electron, and energy transfer in the monopole case gets modified by a factor of β^2 due to Equation (2.28):

$$\left(\Delta p\right)^{mon} = \int_{-\infty}^{\infty} e \cdot E_3^{mon}\left(t\right) dt = \int_{-\infty}^{\infty} e \cdot \beta \cdot E_2\left(t\right) dt = \frac{2e^2}{bc}$$

and therefore

$$\left(\Delta E\right)^{mon}\left(b\right) = \frac{2e^4}{mc^2} \cdot \frac{1}{b^2} \ .$$

It is a common misconception that the additional β factors in monopole/charged particle interactions arise from the Lorentz force law, $\vec{F} = g\left(\vec{B} - c\vec{\beta} \times \vec{E}\right)$. But, as illustrated above, it is due to the electric field of a moving magnetic charge implied by the Lorentz transformation into the rest frame of the atomic electron.

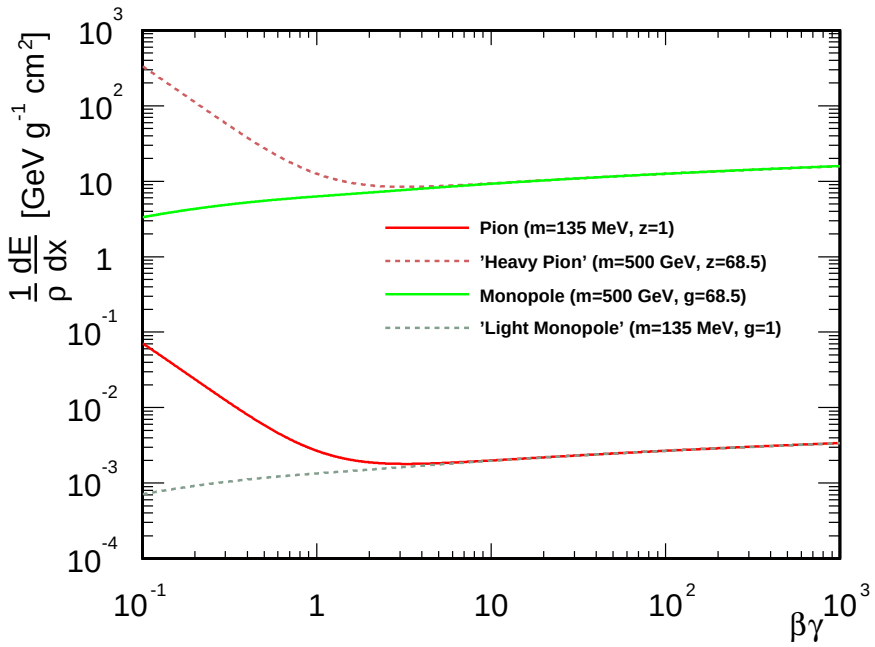

Figure 2.4: Energy Loss for electric and magnetic charges ($I = 100\ eV$)

Applying Equation (2.25), the energy loss due to ionization for magnetic monopoles becomes

$$\frac{1}{\rho}\left(\frac{dE}{dx}\right)_{m\bar{m}} = D\frac{Z}{A}\cdot g^2\cdot\left(\ln\left(\frac{2m_e\beta^2\gamma^2T_{max}}{I^2}\right)-2\beta^2\right) \tag{2.31}$$

and the width of the Gaussian approximation for multiple scattering of a magnetic charge is

$$\theta_0^{m\bar{m}} = \frac{13.6\text{ MeV}}{cp}g\sqrt{\frac{x}{X_0}}\left(1+0.038\ln\left(\frac{x}{X_0}\right)\right) \tag{2.32}$$

In Figure 2.4 and Figure 2.5 energy loss and multiple scattering effects for charged particles and monopoles are compared. The energy loss for fast magnetic charges is about four orders of magnitudes higher than for any single electrically charged particle due to the large contribution of $g^2 \approx 4692$. Scattering angles at the other hand tend to be smaller for monopoles since the angular width is inversely proportional to the particles mass. Monopoles are expected to be heavy and therefore produced with small momentum in the Tevatron; it is interesting that the tendency to ionize decreases for low monopole momenta.

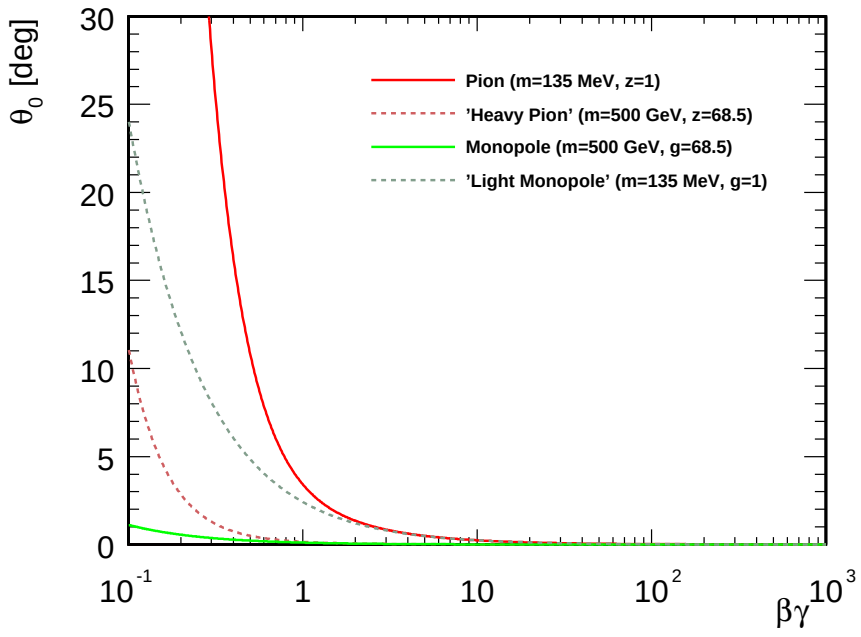

Figure 2.5: gaussian multiple scattering approximation ($x/X_0 = 0.2$)

2.5 Cross-Section of $m\bar{m}$-pairs in $p\bar{p}$-collisions

Despite lively development, as evidenced by the number of recent publications[5, 6, 7], the field theory of magnetic charge is still in a primitive state. The major problem is the large coupling of magnetic monopoles implied by the Dirac Quantization Condition. Due to the large coupling,perturbative theory cannot provide reliable results.. In Reference [7] a nonperturbative quantum field theoretic formulation is proposed and promises reliable cross section calculations for monopole production in the future.

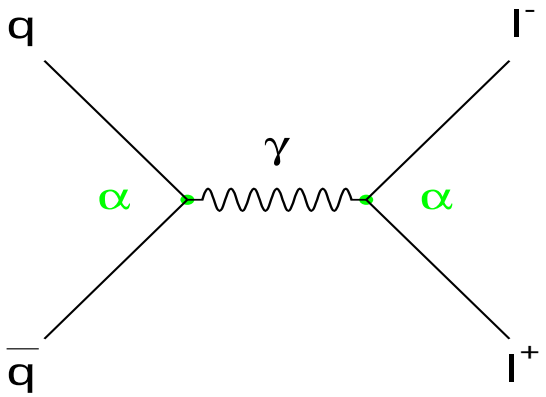

Figure 2.6: Drell-Yan process ...

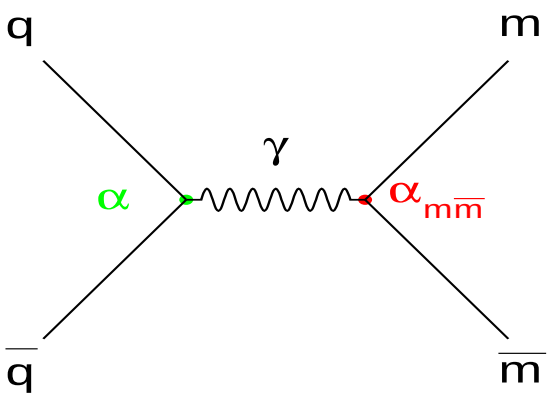

Figure 2.7: ... and monopole production

Throughout this study, monopole/anti-monopole ($m\bar{m}$) pairs are considered to be produced in $p\bar{p}$ collisions in a Drell-Yan like fashion. The Drell-Yan process describes the annihilation of a $q\bar{q}$ pair into a virtual photon which then decays to a pair of arbitrary leptons. Figure 2.6 shows the Feynman diagram for conventional Drell-Yan production, while Figure 2.7 shows the diagram for the similar process producing $m\bar{m}$. The cross sections calculated for this simple production mechanism allow qualitative estimates in the absence of a sound field theoretic formulation of monopole production. Production limits have already been derived this way [8]. Possible future improvements on the dual quantum electrodynamics are expected to put the estimates of monopole production on an even firmer ground [6, 7].

2.5.1 Drell-Yan process

The annihilation of a pair of quarks to a photon which then decays into a pair of leptons is refered to as a Drell-Yan process (see Figure 2.6). The cross section of Drell-Yan depends on the strong interaction between the initial pair of quarks. In the high energy limit, the quarks are treated like free charged particles and the interaction is purely electromagnetic. This is a very good approximation for reasonably high energies $E \gg m_l$, where E is the total energy of the incident particles in the center of mass system. The cross section $\sigma\left(q\bar{q} \to l^+l^-\right)$ is then simply related to $\sigma\left(e^+e^- \to \mu^+\mu^-\right)$, which is given by

$$\sigma\left(e^+e^- \to \mu^+\mu^-\right) = \frac{4\pi\alpha^2}{3E_{cm}^2} \quad , \quad E \gg m_\mu \ . \tag{2.33}$$

The electron charge e is replaced by the quark charge $Q|e|$ and all possible color orientations of the quark pair are averaged:

$$\sigma\left(q\bar{q} \to l^+l^-\right) = \frac{1}{3}Q^2 \cdot \frac{4\pi\alpha^2}{3E_{cm}^2} \ . \tag{2.34}$$

This is the underlying interaction for the process $p\bar{p} \to l^+l^-$. The complete cross section calculation takes into account the quark structure of the proton and antiproton[13], but is not derived here. Equation (2.34) will require a number of corrections but will always have the same dependence on the coupling constant α.

2.5.2 Drell-Yan like Monopole Production

The Drell-Yan cross section, Equation (2.34), can be used to calculate the production of monopole pairs. First, the proper coupling of the magnetic charge to the electromagnetic field has to be incorporated. It is derived by combining the Dirac Quantization Condition as given in Equation (2.21) with the definition of the coupling constant $\alpha \sim e^2$:

$$\alpha_{m\bar{m}} = \frac{ng}{e}\alpha \quad \Rightarrow \quad \sigma\left(q\bar{q} \to m\bar{m}\right) = \left(\frac{ng}{e}\right)^2 \cdot \sigma\left(q\bar{q} \to l^+l^-\right) \ . \tag{2.35}$$

Thus, the Drell-Yan cross section has to be scaled by a factor of

$$(g/e)^2 \approx 4692 \quad , \ n = 1$$

in order to get the monopole pair production cross section.

Furthermore, σ has to be convoluted with β^2 due to the nature of the coupling of magnetic charge to the electromagnetic field [5]. Here β refers to the velocity of the virtual photon in the lab frame. The β^2 factor is due to the same effect in interactions between electric and magnetic charges, that is derived in Section 2.4 for energy loss and multiple scattering. Since quarks are electrically charged particles and the production process therefore describes an interaction between electric and magnetic charge, the β^2 factor has to be included.

For Monte Carlo studies, the monopole pair production cross section is derived by Drell-Yan generation of muons using PYTHIA[10]. The lepton pair in the final state is replaced with an appropriate monopole pair and the computed Drell-Yan cross section is recorded. To properly take into account the kinematic turn-on[8], an additional β-convolution has to be performed. This effect is incorporated by setting the muon mass in PYTHIA to the assumed monopole mass. To include the β^2 convolution, events are rejected based on the gamma's β^2 value. The cross section is modified by the ratio of accepted events to total events:

$$\sigma' = \frac{N_{acc}}{N_{tot}} \cdot \sigma_{DY} \ .$$

Here N_{tot} refers to the total number of muon pairs generated while N_{acc} is the number of events accepted in the β^2-convolution mechanism. This is a statistical method of performing the integration

$$\sigma_{m\bar{m}} = \left(\frac{ng}{e}\right)^2 \int_M^\infty \beta^2 \frac{d\sigma}{dm} dm \ ,$$

where M is the assumed monopole and m the invariant di-monopole mass, without knowing $\frac{d\sigma}{dm}$ but just σ, which is the only quantity delivered by PYTHIA. Note that the β^2-convolution not just cuts down the cross section but also biases the monopole momenta to higher values. This has a positive effect on the acceptance of the Time-of-Flight detector determined in Section 4.4. In the last step the cross section is renormalized according to Equation (2.35):

$$\sigma_{m\bar{m}} = \left(\frac{ng}{e}\right)^2 \cdot \sigma' = \left(\frac{ng}{e}\right)^2 \cdot \frac{N_{acc}}{N_{tot}} \cdot \sigma_{DY} \ . \tag{2.36}$$

The Drell-Yan cross section is shown in Figure 2.8 and Table 2.1 for various assumed monopole masses. Figure 2.9 illustrates the differential cross section for a projected monopole mass of 200 GeV.

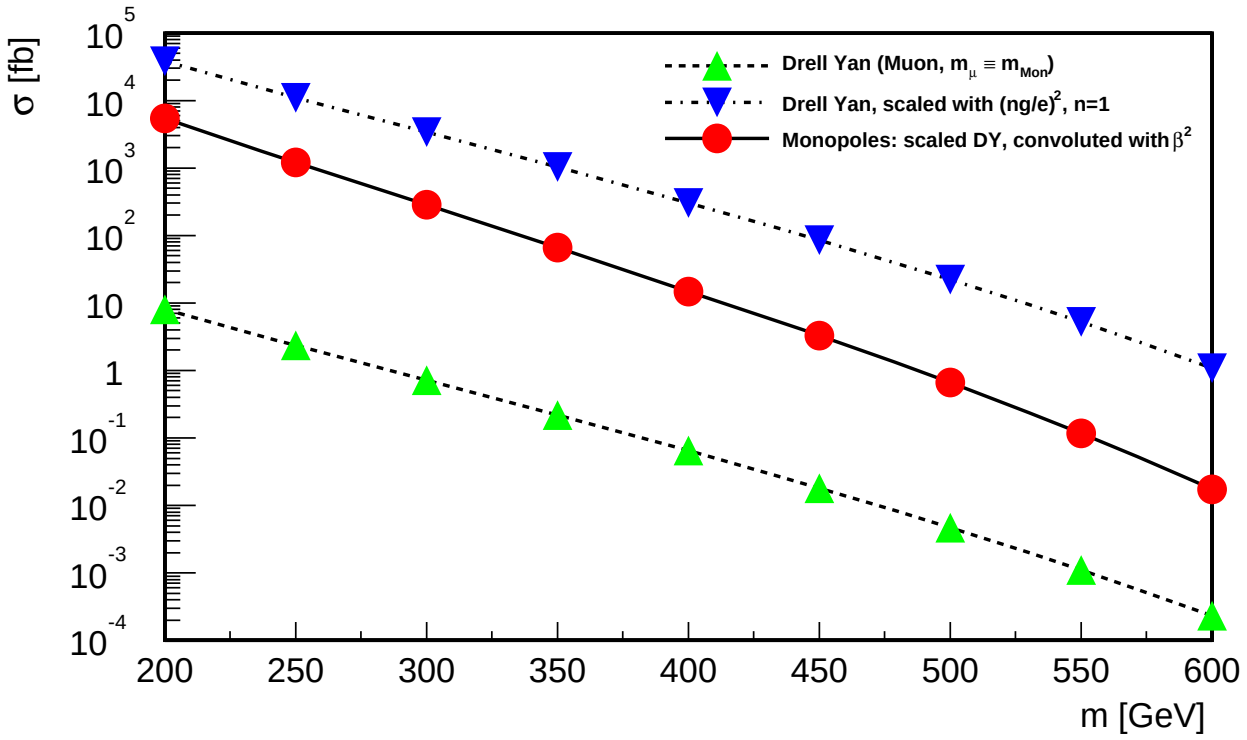

Figure 2.8: Cross section for proposed Drell-Yan like pair production of magnetic monopoles

m [GeV]	σ_{DY} $[fb]$	σ_{DY}^{scaled} $[fb]$	$\sigma_{m\bar{m}}$ $[fb]$
200	8.0570	37805.50	5460.790
250	2.3560	11054.90	1200.480
300	0.7198	3377.48	283.308
350	0.2183	1024.32	66.442
400	0.0646	303.12	14.862
450	0.0182	85.16	3.307
500	0.0047	22.08	0.659
550	0.0011	5.23	0.118
600	0.0002	1.08	0.017

Table 2.1: Drell-Yan and monopole cross sections

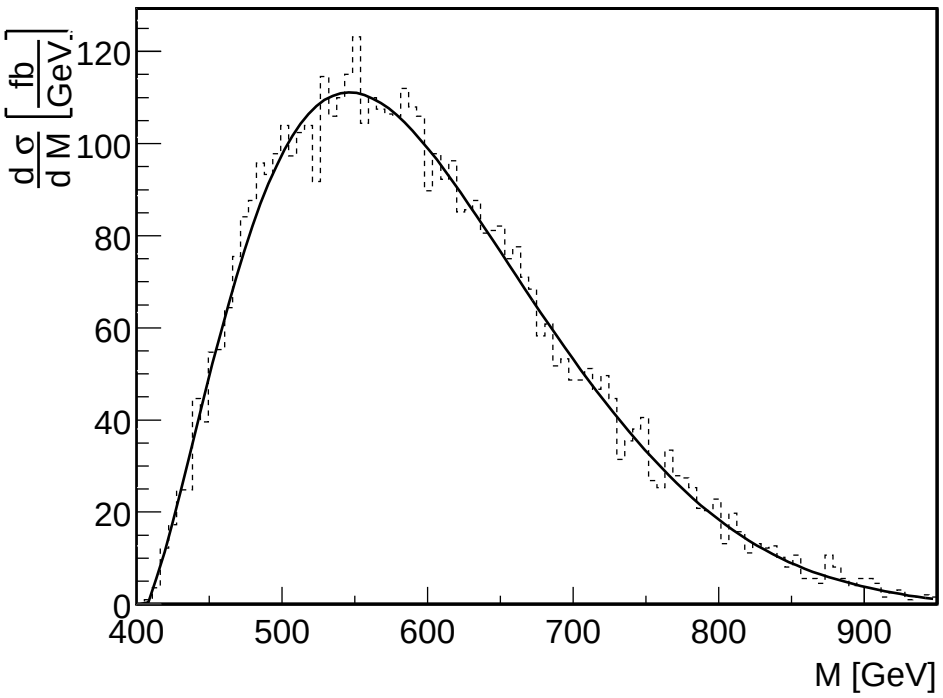

Figure 2.9: $\frac{d\sigma}{dM}$ for m=200 GeV; M represents the invariant virtual photon mass

Chapter 3

Experimental Setup

3.1 The Tevatron Collider

The Tevatron proton-antiproton Collider is the highest-energy particle collider currently operational anywhere in the world. It began operation in 1983 and has since served as a major component for breakthrough discoveries in the field of elementary particle physics. The most important of those has been the discovery of the top-quark in 1995, one of the building blocks of the Standard Model of fundamental particles. Throughout the years the accelerator underwent several upgrades to keep up with the technical requirements set by the respective physics goals. After an upgrade period of more than six years, the Tevatron Collider gone back in operation in March 2001 seeking to advance our knowledge of physics in new dimensions.

The most important feature of the new configuration is the introduction of the Main Injector, a rapid cycling proton synchrotron with a circumference half that of the Tevatron. Protons are injected from the Booster (another synchrotron) at 8 GeV and are accelerated to either 120 GeV if transfered for the antiproton target or 150 GeV if injected to the Tevatron. The antiprotons are produced by 120 GeV protons incident on a nickel target. They are collected in a debuncher ring at 8 GeV, and transfered to the accumulator where they are stochastically cooled. The resulting antiproton bunches are transfered to the Recycler ring before they are eventually accelerated in the Main Injector and Tevatron to the final energy of 980 GeV. The Recycler is an 8 GeV permanent magnet machine equipped with stochastic

cooling and capable of capturing antiprotons after the end of a store. This significantly enhances the number of antiprotons available under normal operation and thus the luminosity.

The design luminosity of the upgraded Tevatron is $1.0 \times 10^{32} cm^{-2} s^{-1}$ while colliding 36 proton on 36 antiproton bunches at a center of mass energy of 2 TeV. Each bunch has an approximate length of 30 cm and carries about $270 \times 10^9/70 \times 10^9$ (protons/antiprotons) particles. The bunches cross each other at a rate of 2.5 MHz where it takes about 396 ns between each crossing. To further increase the luminosity in the second phase of the experiment (Run IIb) by roughly a factor of 2, it is planed to lower the timespan between crossings to about 132 ns while colliding 108 on 108 bunches. The Tevatron is expected to deliver 2 fb^{-1} integrated luminosity during the first two years and further 13 fb^{-1} during the following five years (Run IIb). This increase of luminosity with respect to Run I (110 pb^{-1}) represents a major improvement, fostering the hope for new physics discoveries in upcoming years.

The Tevatron delivers its $p\bar{p}$ beam to two multipurpose particle detectors, the D0 and the CDF detectors. The CDF Experiment will be described in Section 3.2.

3.2 The CDF Detector

3.2.1 Overview

CDF[16] (Collider Detector at Fermilab) is one of two multipurpose particle detectors studying $p\bar{p}$-collisions delivered by the Tevatron, and was built in the early 80's. The dramatically increased rate of events in Run II demanded a redesign of the veteran apparatus to match the standards set by the improved parameters of the accelerator. In Figure 3.1 an isometric view of the detector is shown. It is designed to have an approximately cylindrically symmetric layout of detector components with uniform segmentation in η and ϕ whenever feasible. In general, the detector can be categorized into three layers: high resolution tracking on the inside, electromagnetic and hadronic calorimetry in the middle, and muon identification on the outside. In the following, each of those will be shortly discussed.

The superconducting solenoid provides a constant magnetic field of 1.4 T and contains

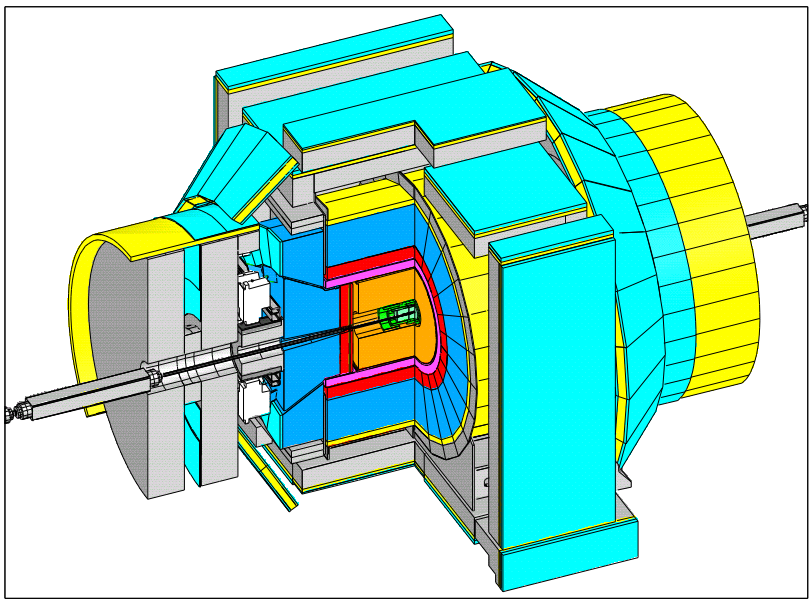

Figure 3.1: Isometric view of the CDF detector

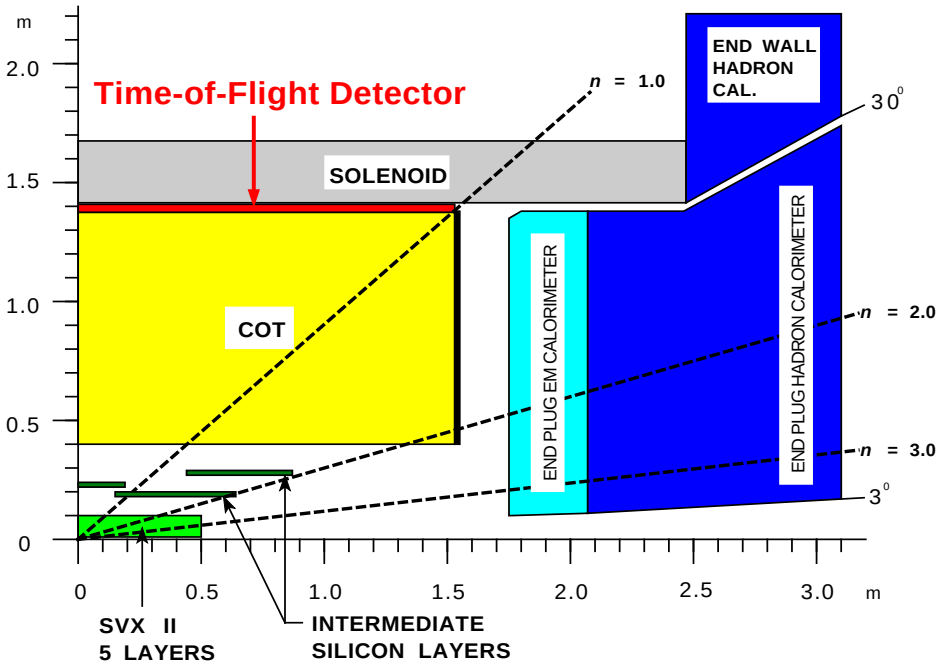

Figure 3.2: Sectional view of CDF, including the integrated tracking system

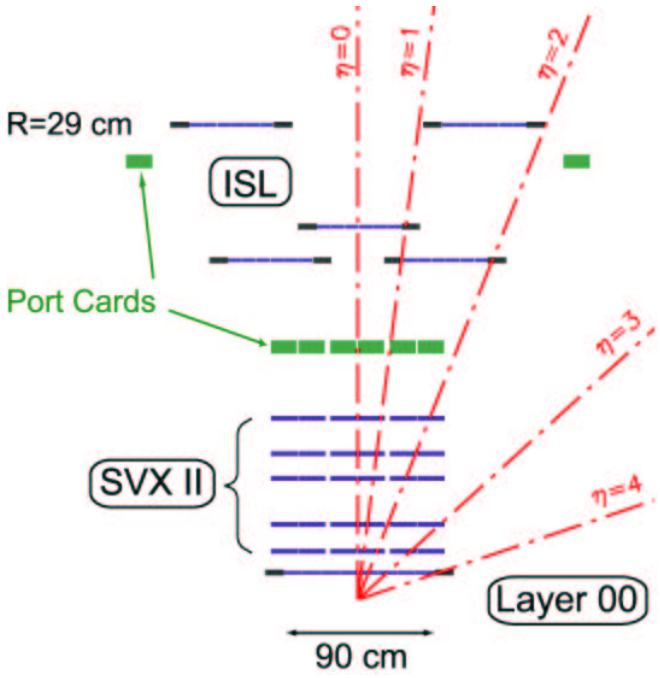

Figure 3.3: Side view of the silicon tracking system

the "integrated tracking system", which refers to a number of different detectors suitable for charged particle tracking. This system is illustrated in Figure 3.2. The tracking at low radii is performed by a sophisticated system of silicon layers (Figure 3.3) designed to provide good angular coverage as well as precise 3-dimensional track impact parameter determination.

The Silicon Vertex Tracker (SVX II) consists of five layers composed of double sided silicon sensors. It is built in three cylindrical barrels with a total length of 96 cm, covering $\sim 2.5\sigma$ of the luminous region, which is determined by the bunch lengths of the colliding beams. Its resolution performance is greatly improved by the addition of another silicon layer inside of the SVX II installed directly onto the beam pipe, called "Layer 00". Since radiation damage will limit their lifetime, the silicon sensors will have to be replaced after approximately 2-3 years. The intermediate silicon layers (ISL) enhance the z resolution of the silicon system and bridge more seamlessly between vertex detector and outer tracker. Moreover, these stand-alone silicon segments allow integrated tracking algorithms which maximize the tracking performance over the region $|\eta| < 2.0$.

The Central Outer Tracker (COT) is an open cell drift chamber which covers radii between

44 cm and 132 cm. In order to limit drift times to less than 100 ns as required by the Tevatron bunch-crossing, small drift cells and a fast gas (Ar-Ethane-CF_4) are used. The COT consists of 2520 basic cells each of which has a line of 12 sense wires alternating with field shaping wires. The wires run down the middle of two gold-on-mylar cathode planes, which like the wires themselves, are strung between two endplates. A fast digitization of the COT signal is used by the extreme Fast Tracker (XFT), which uses look-up tables as a simple tracking algorithm to identify high-momentum charged tracks at Level-1. The XFT allows to trigger on tracks at Level-1, one of the most significant improvements of the detector. The complete digitization of the COT measurement serves track reconstruction and momentum determination at Level-3.

A Time-of-Flight system has been newly installed between the outer limits of the COT and the solenoid. Since it represents on of the most important parts of CDF for a direct magnetic monopole search, it will be described in greater detail in Section 3.2.2.

The region $|\eta| \leq 2.5$ behind the solenoid is covered with both electromagnetic and hadronic scintillator-based calorimetry. The EM calorimeter is a lead/scintillator sampling device with a unit layer composed of 4.5 mm lead and 4 mm scintillator. It features 23 layers for a total thickness of about 21 interaction lengths at normal incidence. A hadronic calorimeter unit layer consists of 5 cm iron and 6 mm scintillator; The total thickness of the hadronic calorimeters is 4.5 and 7 nuclear interaction lengths in the central and Plug region respectively. The ability to match tracks with projective towers and shower position in the central region is a powerful tool for CDF analysis.

CDF II can detect muons in the region $|\eta| \leq 2.0$ using a system of proportional chambers and scintillators. Geometry issues and maximal possible coverage led to the use of four different systems:

- Central Muon Unit (CMU, $|\eta| \leq 0.6$)
- Central Muon Upgrade (CMP, $|\eta| \leq 0.6$)
- Central Muon Extension (CMX, $0.6 \leq |\eta| \leq 1.0$)
- Intermediate Muon Unit (IMU, $1.0 \leq |\eta| \leq 1.5$).

Between $|\eta| = 1.5$ and $|\eta| = 2.0$ there is also muon identification, with granularity insufficient for triggering but enabling identification of high p_T tracks in this region as muons. All muons are identified by their penetrating properties through material, and have their momentum measured using the integrated tracking system contained in the solenoid. The muon units consist of drift chambers which are located outside substantial steel absorber. The systems are supported by scintillation counters in order to improve timing information and cosmic rejection. Triggering and reconstruction of muons will be at the core of several physics goals of the upcoming CDF era.

It will become clear in Chapter 4 that magnetic monopoles, due to their highly ionizing signature, are not expected to reach any detector outside the central region of the solenoid. Since the monopole trigger is proposed to make use of the Time-of-Flight system which is located just inside the magnet, no information from calorimetry or muon system is to be expected. Although the plug calorimetry ($|\eta| \leq 1.0$ might have reasonable acceptance for magnetic charges, no such approach is considered in this document.

3.2.2 Time of Flight System

In order to enhance its particle identification capability, the CDF detector has been instrumented with a Time-of-Flight[17] system for Run II. Though its original motivation has been mainly to increase the sensitivity of CP violation and B mixing measurements, it turns out to be an ideal tool for a magnetic monopole trigger because of the highly ionizing signature of magnetic charge (Section 2.4). It is the main concept of this document to trigger on large pulses in the TOF system for the search of magnetic monopoles.

The CDF II TOF system consists of 216 bars of fast scintillator (Bicron BC-408), 3.0 m in length, arranged in a cylinder inbetween the COT chamber and the solenoid magnet. Its location is illustrated in Figure 3.2. Three bars are mechanically assembled together to form a so called "three-pack". They are wrapped in several layers of different materials to make them lightproof and provide mechanical stability. Each three-pack features a set of built-in optical fibers which enable calibration and testing using laser light. In order to minimize cracks between them, when assembled in a cylinder, each bar has a slightly trapezoidal cross

section.

Photomultiplier tubes (PMT) are mounted on both ends of each bar, and their signals are boosted by a preamplifier. The space constraints imposed on the TOF system are strictly limited. It has to be operated within the solenoid, this including PMT's and preamplifiers. This raises issues concerning the effect of the magnetic field on the performance of the PMT's. Due to fact that PMT gains are substantially reduced in magnetic field the PMT's must have high gain. The TOF Front End Electronics rely upon the CDF calorimeter ADC/Memory (ADMEM) boards, but with custom built charge and time digitization for TOF phototube pulses. Though some modifications were necessary to the standard CDF electronics, this had the advantage of benefiting from a significant existing base of technology already in place and working.

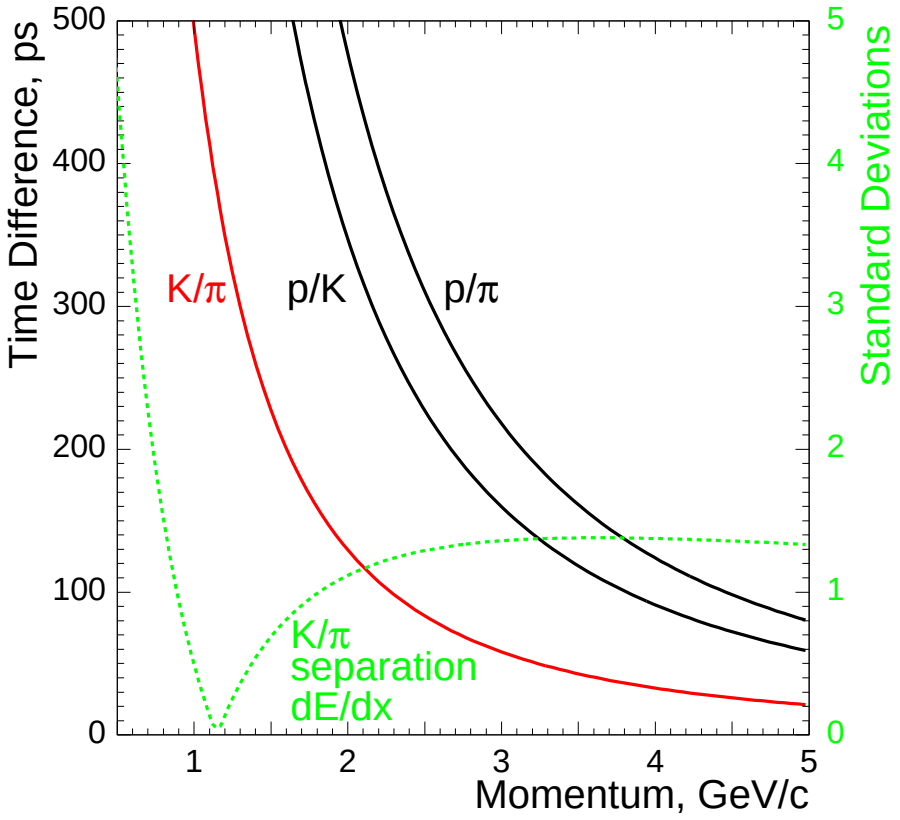

Figure 3.4: Particle Identification with the TOF system

The immediate objective of the TOF electronics is to provide timing signals of particles

exciting the scintillator, which is realized by time-to-amplitude digital conversion. However, to obtain the most precise time measurement it is necessary to apply "pulse height" corrections. Therefore, the readout electronics also provide a measurement of the charge produced by the PMT pulse. In fact, the magnetic monopole trigger intends to make use of nothing but the charge information, since it correlates with the energy loss due to ionization. The Time-of-Flight signal path and read-out electronics will be described in greater detail in Chapter 6, when the trigger strategy is presented.

The main purpose of the Time-of-Flight system is particle identification through a precise flight time measurement. The CDF TOF system provides a time resolution of $\sim$ 100 ps. Figure 3.4 illustrates how different particles like kaons, pions, and protons can be separated by their different flight times. The capability to seperate kaons and pions through $\frac{dE}{dx}$ information obtained from the charge measurement is also shown. This particle identification capability extends CDF's ability to determine the flavor of the b quark and to identify the b hadron decay products substantially.

3.2.3 Trigger and DAQ

The trigger plays an important role in hadron collider experiments since the collision rate is much higher than the rate at which data can be stored on tape. Due to the drastic increase in luminosity and decrease in bunch-crossing time, the trigger and DAQ systems had to undergo substantial upgrades in order to be capable of handling the large data transfer rates in Run II. One bunch crossing produces on average one collision and a crossing occurs at a rate of 7.6 MHz. On the other hand, only about 100 events can be written to mass storage per second. A sophisticated trigger system is therefore necessary to handle the crossing rate of 7.6 MHz by rejecting events which appear not to be interesting in light of the physical goals of the experiment. The trigger system consists of three levels with each level providing a rate reduction sufficient to allow processing in the next level with minimal deadtime. Its architecture is illustrated in Figure 3.5.

The Data Acquisition System (DAQ) is responsible for collecting data fragments from front-end electronics systems for events accepted by the Level-2 trigger and transfering them

to the Level-3 trigger system. Events accepted by the Level-3 trigger are sent to mass storage, for eventual analysis.

Level-1

The first trigger level has to accommodate a bunch-crossing period of 132 ns and a decision time of 4 μs. It accomplishes these requirements by fully pipelining all front-end electronics with on-board buffers for 42 beam crossings. At Level-1 data from the calorimeters, COT chamber, and muon detectors help reject uninteresting $p\bar{p}$ collisions and thereby reduce the event rate from $\sim$ 7.6 MHz to less than 50 kHz. The TOF trigger proposed here will also be implemented at this level. It will be discussed separately in Chapter 6 in more detail. The Level-1 trigger is a synchronous system with each decision reaching the front-end card at the end of the pipeline (Figure 3.5). Its most significant upgrade with respect to Run I is the addition of track finding, a Level-2 decision in Run I.

Level-2

The events accepted by Level-1 will be transfered into one of 4 Level-2 buffers where another decision will be asynchronously made within $\sim$ 20 μs, further reducing the event rate to approximately 300 Hz. The four buffers are sufficient to average out the rate fluctuations and allow a 40 kHz input rate from Level-1 with $\leq$ 10% deadtime. All of the information used in Level-1 decision is available to the Level-2 system, but with higher precision. Other detector components will now be included in the Level-2 decision, i.e. silicon tracking (SVX II) information. The Silicon Vertex Tracker (SVT) enables one to use impact-parameter information at Level-2 in order to detect secondary vertices and thereby further increases the physics reach of the experiment substantially.

Level-3

Events accepted by Level-2 are transfered through a commercial ATM network switch to the Level-3 farm, a 250 Linux nodes computer network. The Level-3 algorithms take advantage of the full detector information and the improved resolution not available to the lower trigger

levels. The Level-3 subsystem fully reconstructs and partially analyzes the event before passing it to the Data-Logger subsystem in case of a Level-3 accept.

Mass Storage

The Data-Logger takes care of the mass storage of Level-3 accepted events and writes them on tape. It furthermore provides online monitoring to verify that detector, trigger and data acquisition are working correctly. The number of events to be recorded is 900 million per year. This means $\sim$ 250 TB[1] per year for raw data, and $\sim$ 140 TB per year for reconstructed event data. Together, it will take about 500 TB per year to store all this information.

[1] 1 TB = 1 terabyte = $1 \cdot 10^12 bytes$

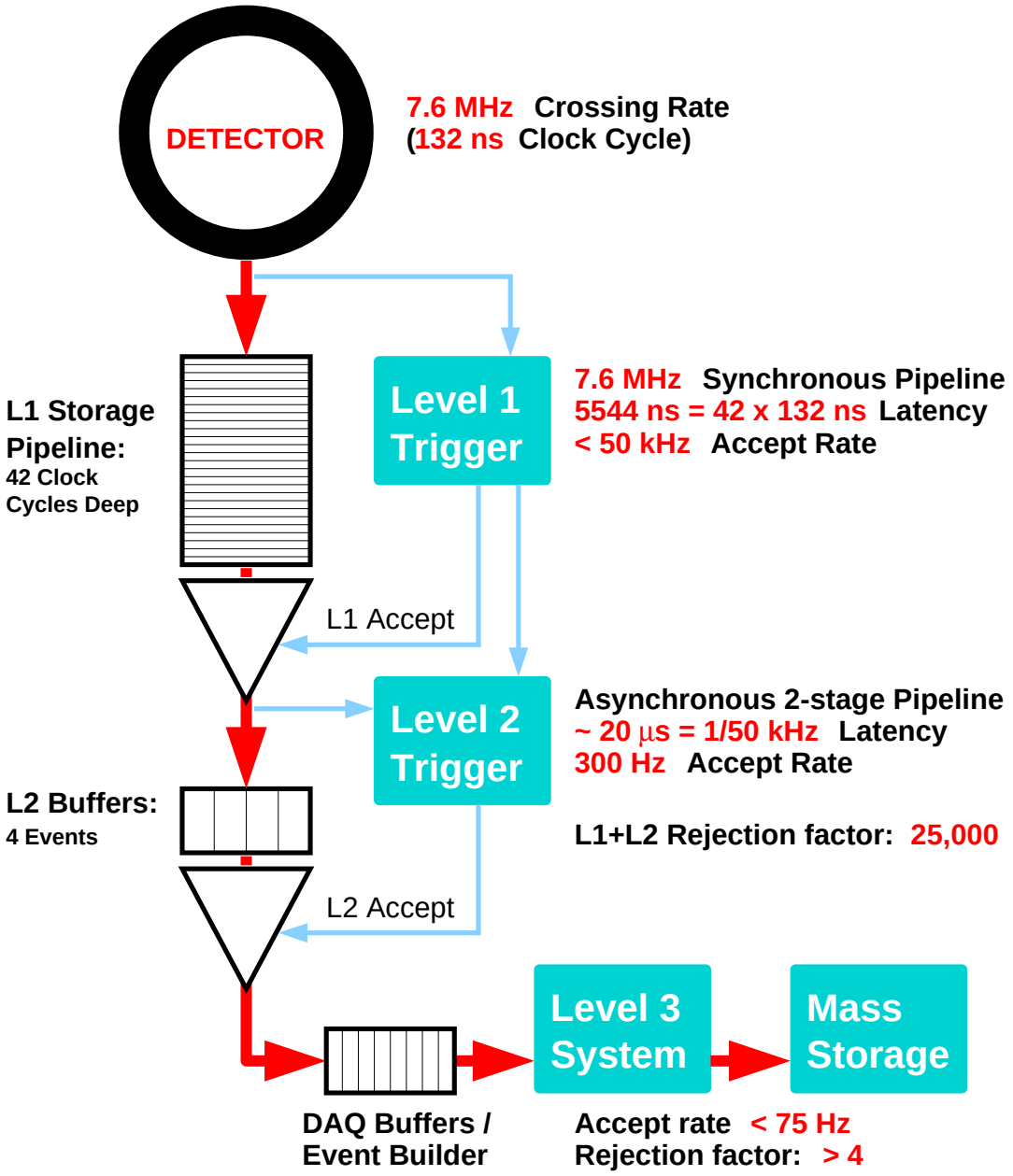

Figure 3.5: CDF II data flow

Chapter 4

Simulation of monopoles in CDF

4.1 Introduction

A stand-alone program has been designed which takes the monopole pairs generated according to Section 2.5.2 and tracks each monopole through a simplified geometry of the CDF detector. It assumes a constant magnetic field of $-1.4116 \cdot \vec{e}_z$ inside the integrated tracking system ($r \approx 145.0\ cm$). The kinematics of a magnetic monopole in this configuration as presented in Section 2.2 have been taken into account as well as effects of multiple scattering and energy loss, which are described in Section 2.4. The later two are discussed in Section 4.2 and Section 4.3 respectively while Section 4.4 covers the determination of the acceptance ϵ_a of the Time-of-Flight detector.

To simulate energy loss and multiple scattering, a simplified geometry of the CDF detector is implemented. A list of all detector systems that are taken into account is shown in Table 4.1. The set of material constants contributing to the energy loss and multiple scattering has been adapted from the GEANT [9] software and is listed in Table 4.2. Both effects are evaluated at certain points along the monopole trajectory. The step size is calculated at each step based on the current detector system boundaries and a maximum relative energy loss allowed per step, $\Delta E/E_{kin} \leq 0.25$. Energy loss fluctuations are completely neglected in this model.

Figure 4.1, Figure 4.2, and Figure 4.3 visualize monopole trajectories simulated for 10 arbitrary $m\bar{m}$ events featuring a monopole mass of 500 GeV. The plots also illustrate the

Nr.	Detector	Material	Nr.	Detector	Material
1	AirEnvironment	Air	17	ISL Midleft a	Silicon
2	SiliconLayer00 a	Silicon	18	ISL Midleft b	Silicon
3	SiliconLayer00 b	Silicon	19	ISL Midright a	Silicon
4	SVX II Layer0 a	Silicon	20	ISL Midright b	Silicon
5	SVX II Layer0 b	Silicon	21	ISL Outleft a	Silicon
6	SVX II Layer1 a	Silicon	22	ISL Outleft b	Silicon
7	SVX II Layer1 b	Silicon	23	ISL Outright a	Silicon
8	SVX II Layer2 a	Silicon	24	ISL Outright b	Silicon
9	SVX II Layer2 b	Silicon	25	COT	Ar-Ethane-CF4
10	SVX II Layer3 a	Silicon	26	COTInnerCylinder	COTInnerCylinder
11	SVX II Layer3 b	Silicon	27	COTOuterCylinder	Aluminum
12	SVX II Layer4 a	Silicon	28	COT Left EndCap	Aluminum
13	SVX II Layer4 b	Silicon	29	COT Right EndCap	Aluminum
14	Hybrid	Hybrid	30	Time-of-Flight	Scintillator
15	ISL Center a	Silicon	31	Solenoid	SuperConducter
16	ISL Center b	Silicon			

Table 4.1: List of CDF detector systems considered in the simulation

geometry of the Time of Flight System. Green and thick trajectories mark monopoles accepted by the TOF Detector. The significant signature of a magnetic charge track, its linear course in the transverse and its parabolic shape in the longitudinal plane, suppressed by relativistic effects, can be seen.

Material	ρ $[\frac{g}{cm^3}]$	$\frac{Z}{A}$	I [GeV]	X_0 [cm]
Air	1.205e-3	0.49919	$0.957438 \cdot 10^{-7}$	30423.2
Scintillator	1.032	0.61444	$0.103968 \cdot 10^{-6}$	42.4
Aluminum	2.7	0.482	$0.160942 \cdot 10^{-6}$	8.9
Ar-Ethane-CF_4	0.00178	0.45	$0.215707 \cdot 10^{-6}$	11000.0
Silicon	2.33	0.48443	$0.172042 \cdot 10^{-6}$	9.36
COTInnerCylinder	1.625	0.5055	$0.736025 \cdot 10^{-7}$	27.4521
SuperConductor	0.8	0.4815	$0.160942 \cdot 10^{-6}$	31.3308
Hybrid	7.8	0.5	$0.103968 \cdot 10^{-6}$	10.1516

Table 4.2: Material constants taken from GEANT

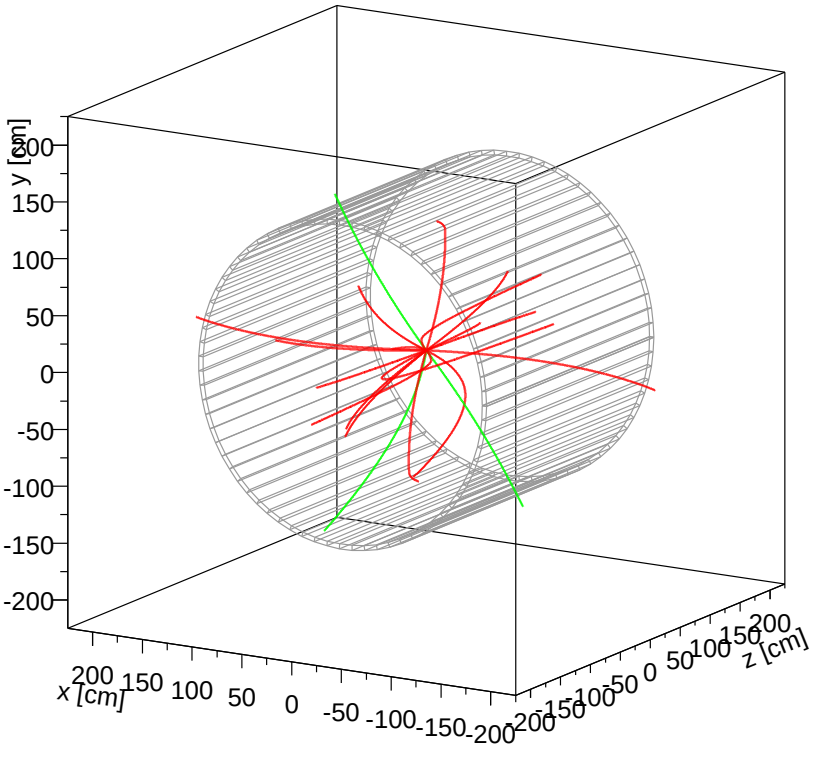

Figure 4.1: Ten $m\bar{m}$ events (m=500 GeV) and the Time-of-Flight system; TOF accepted particles are green and thick

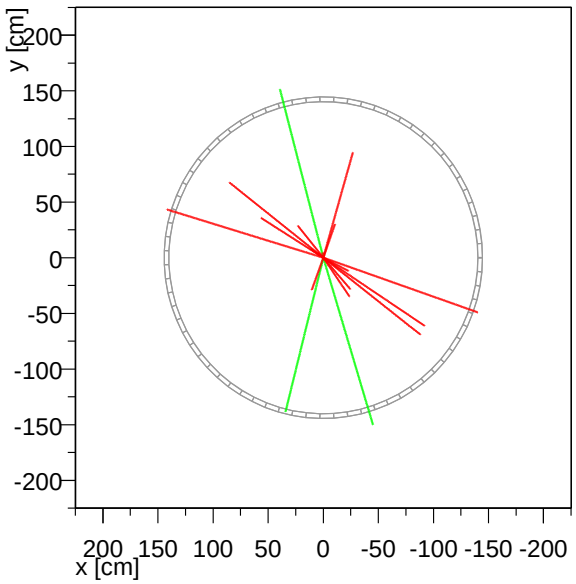

Figure 4.2: Transversal view of ten $m\bar{m}$ events

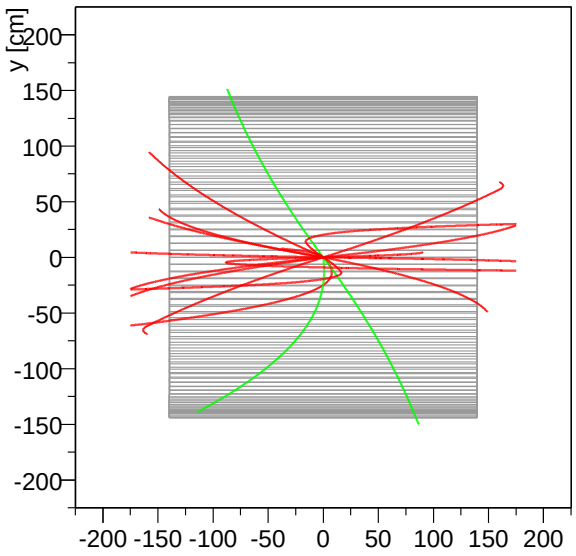

Figure 4.3: Longitudinal view of ten $m\bar{m}$ events

4.2 Multiple Scattering Effects

Figure 4.4 shows the total scattering angle distribution for monopole masses of 200 GeV and 600 GeV and $n = 1$ in the ϕ-plane. The values refers to the angle between the initial momentum and the momentum when the particle enters a scintillator bar. n is the Dirac quantum number according to the Dirac Quantization Condition. Only TOF accepted particles are considered. The histogram for 200 GeV monopoles is scaled to represent the same number of particles like the 600 GeV histogram. As projected in Section 2.4, the influence of multiple scattering is small. The linear course of the monopole track in the transverse plane is not affected. Since the scattering angles increase linearly with the Dirac quantum number n and therefore remain small for $n = 2, 3$. Therefore, the signature of magnetic charge in the integrated tracking system of CDF is not affected by multiple scattering effects at all.

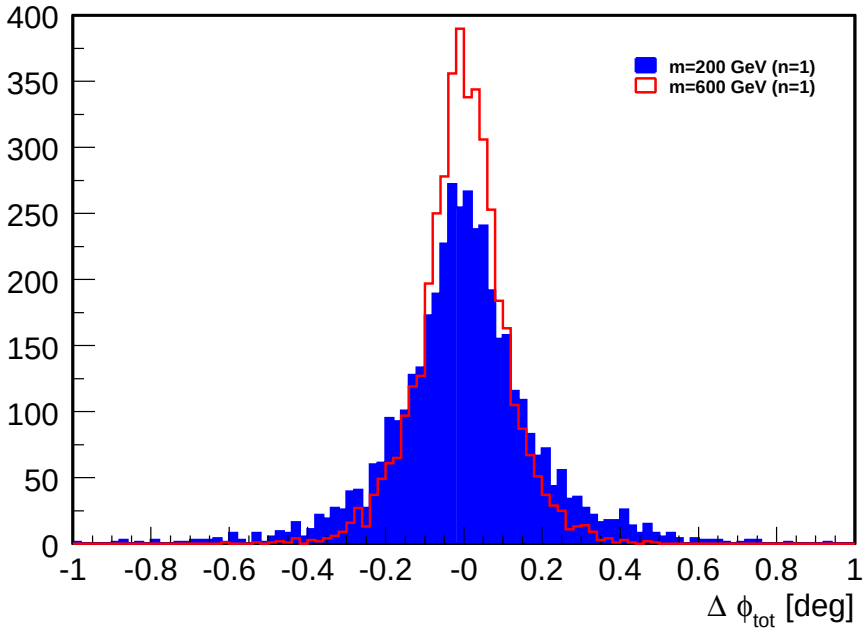

Figure 4.4: Total multiple scattering angles for 200 GeV and 600 GeV monopoles for $n = 1$ in ϕ-plane. The values refer to the angle between the initial momentum and the momentum when entering a Time-of-Flight bar. Only TOF accepted events are considered and the 200 GeV histogram is scaled to represent the same number of particles as the 600 GeV histogram

4.3 Energy Loss Effects

The energy loss of magnetic charge in the CDF integrated tracking system affects the acceptance of the Time-of-Flight detector. Clearly, a monopole can not reach the scintillation counters, if it lost all its energy at lower radii. But even if it looses just a fraction of its initial energy, the magnetic field might carry the monopole outside the geometrical limits of the TOF system due to energy lost in traversed material. Due to the high coupling of magnetic charge, the energy loss due to ionization is large and must be considered in order to perform a realistic simulation of TOF acceptance. Furthermore, the energy deposition of magnetic monopoles in the scintillator is studied, since there is a yet to be investigated correlation between the energy deposited and the pulse height of the measured signal. Finally, the relative energy loss in the superconducting solenoid and the COT end caps, which are made of aluminum and define the longitudinal limits of the COT, are determined in order to make predictions on the feasibility of detectors outside the solenoid.

All presented histograms but Figure 4.11 consider TOF accepted particles only. If histograms are compared for a different choice of monopole mass, the histograms are scales to represent the same number of particles.

Figure 4.5 and Figure 4.6 show the absolute and relative energy loss distributions *before* hitting a scintillator bar, respectively. The quoted energies are the ones deposited in the penetrated materials. Note that these energies are greater than the difference between initial and final energies, since the particles pick up energy in the magnetic field. For $n = 1$, the amount of energy loss due to ionization effects in the integrated tracking system is substantial but cuts down the TOF acceptance by no more than 6 percent. Due to the n^2 dependence of the charge, monopoles with larger numbers of n tend to get stuck at low radii.

Figure 4.7 shows the energy deposition of magnetic monopoles in the TOF scintillators. The energy deposition is huge, much larger than for any other particle known to be produced in $p\bar{p}$ collisions. It remains to be investigated though, how this large energy deposition translates into the trigger defining TOF readout signals. Probably the monopole passing through the scintillation counter causes saturation in the preamplifier, or at least a large signal. A realistic

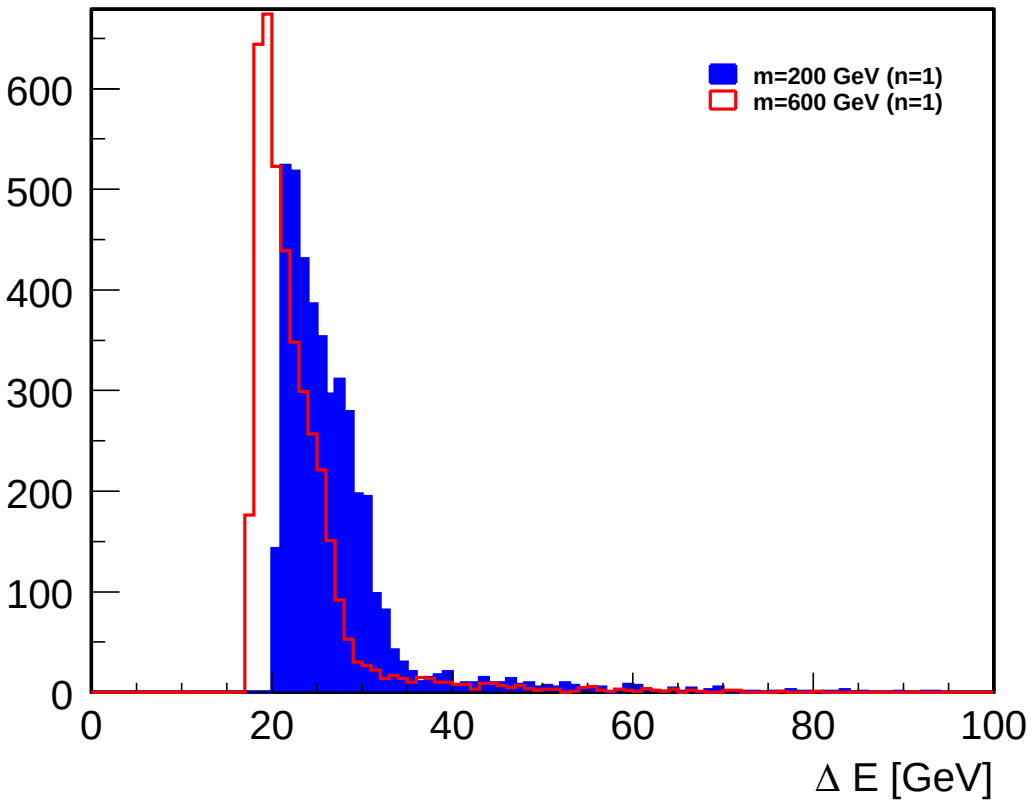

Figure 4.5: Absolute energy loss due to ionization of TOF accepted 200 GeV and 600 GeV monopoles in the integrated tracking system. The quoted energies refer to the sum of energy losses at all points of the trajectory with lower radii than the inner radius of the Time-of-Flight detector. This is larger than the difference between the initial and final energies, since monopoles pick up energy in the magnetic field.

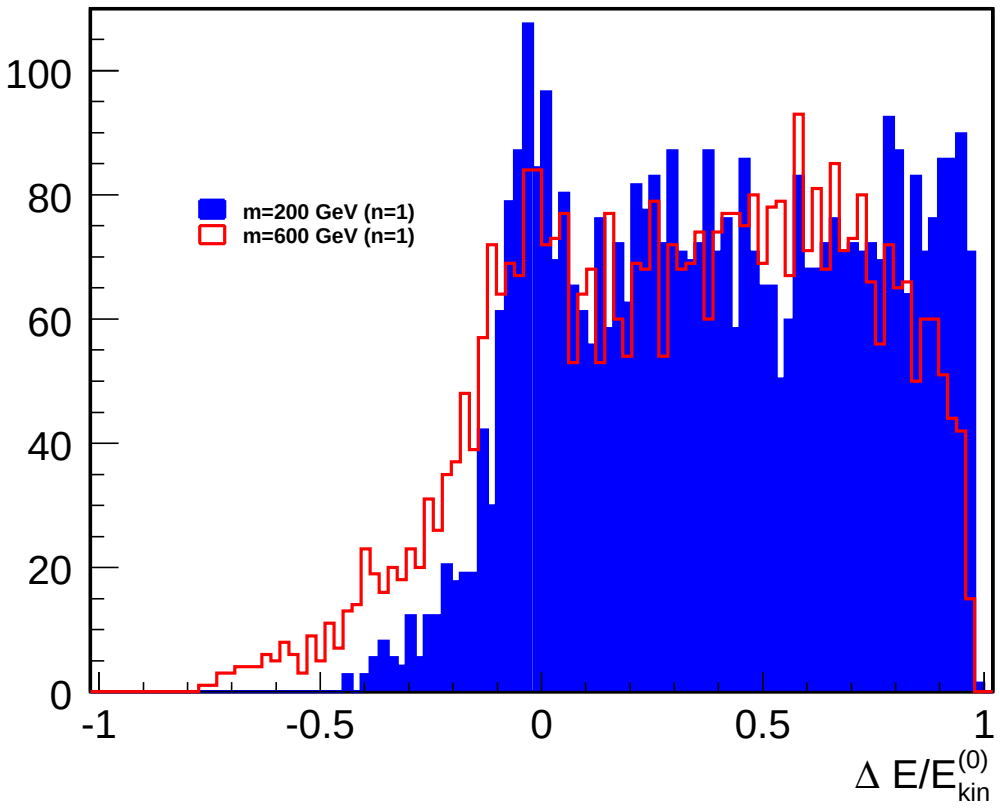

Figure 4.6: Relative energy loss of TOF accepted 200 GeV and 600 GeV monopoles in the integrated tracking system. The energy gain in the magnetic field is included when $\Delta E = E_f - E_0$ is calculated. E_f refers to the energy of the particle before entering the scintillator.

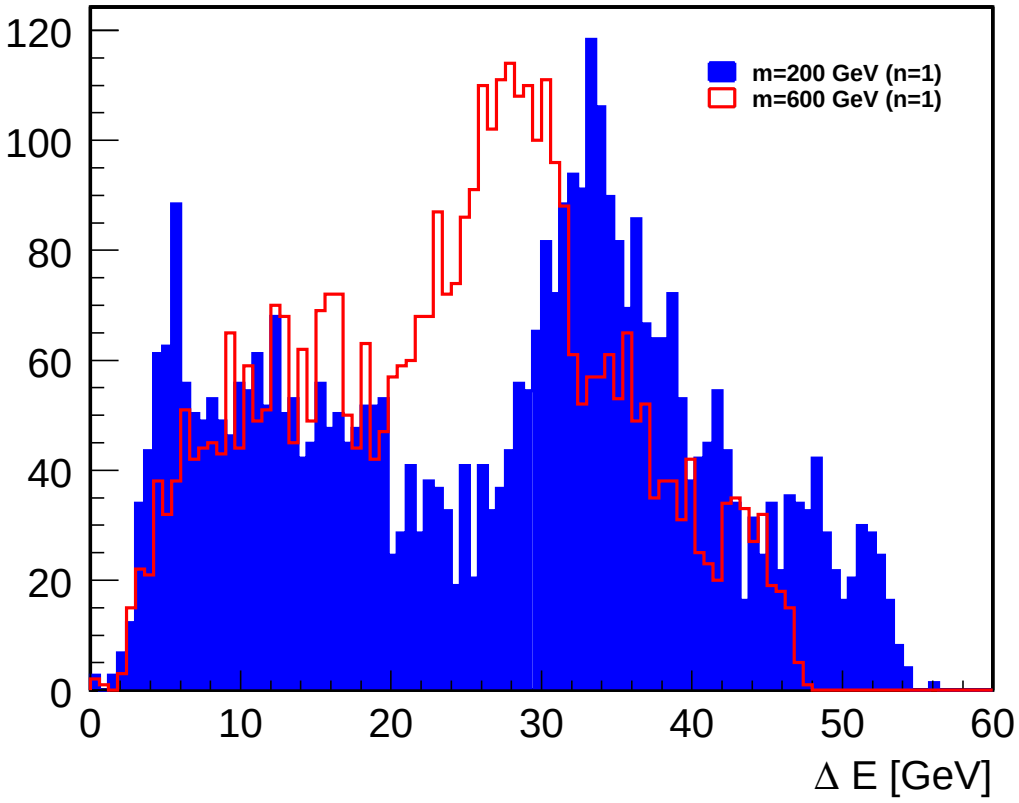

Figure 4.7: Energy deposition of 200 GeV and 600 GeV monopoles in the Time-of-Flight detector. The low energy and high energy peak for each distribution refer to particles which deposit all their energy in the bar and those which do not,respectively. Figure 4.8 and Figure 4.9 show the seperated spectra.

simulation of the TOF readout electronics is under construction but not yet in place and will help to investigate this issue in the near future.

Figure 4.10 depicts the relative energy loss in the solenoid of monopoles which managed to penetrate the scintillator. The rate of particles traveling through the magnet is negligible, which implies that monopoles are not detected in the central calorimeter. The Time-of-Flight system is probably the only place to allow for a triggerable sign.

To search for monopoles in the forward region of the detector seems tempting at the first glance since the magnetic field bends many monopole trajectories along the beamline.

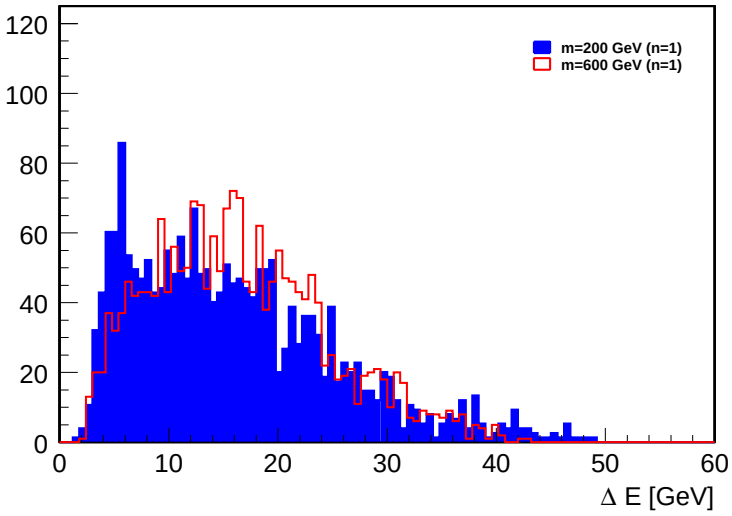

Figure 4.8: Energy deposition of 200 GeV and 600 GeV monopoles in the Time-of-Flight detector for particles which deposit all their energy in the scintillation counter.

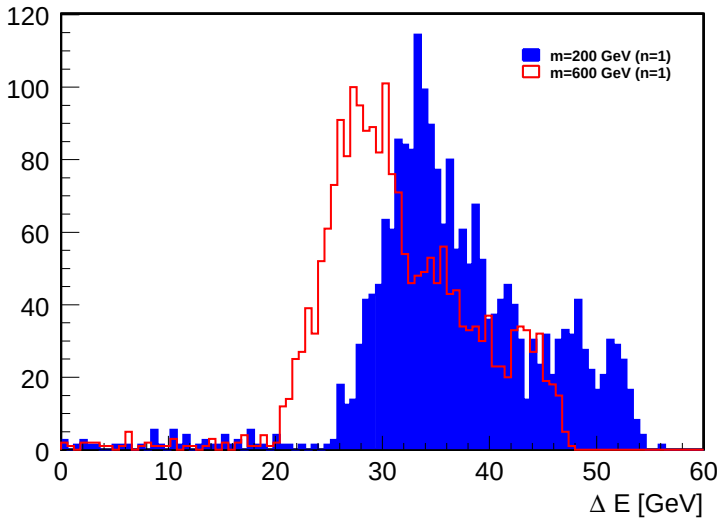

Figure 4.9: Energy deposition of 200 GeV and 600 GeV monopoles in the Time-of-Flight detector for particles which do *not* loose all their kinetic energy in the scintillation counter. The path length of the particle within the bar, which is determined by the entry angle, is the dominant factor.

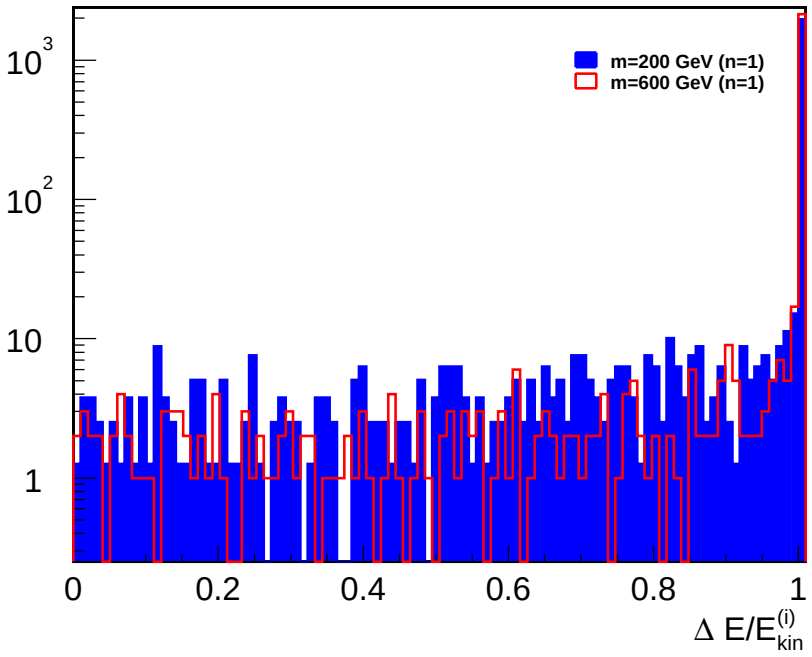

Figure 4.10: Relative energy loss of 200 GeV and 600 GeV TOF accepted monopoles in the solenoid. The solenoid shields magnetic charge from the central calorimeter.

Figure 4.11 illustrates that the COT endcaps lower the rate of magnetic charge reaching any detectors in this region considerably. The EM sampling calorimeters are possibly not sensitive to magnetic charge, since most likely all the monopole's energy would be deposited in the first layer of lead. The most compelling argument against a monopole search in the CDF forward region is, that monopoles accepted in this part of the detector do not cause a clear signal in the tracking system, especially the COT. While calorimeters as well as the TOF detector can produce evidence suitable for a trigger, they can not discover them. A discovery requires the reconstruction of the track with its unique parabola-like shape in the longitudinal plane.

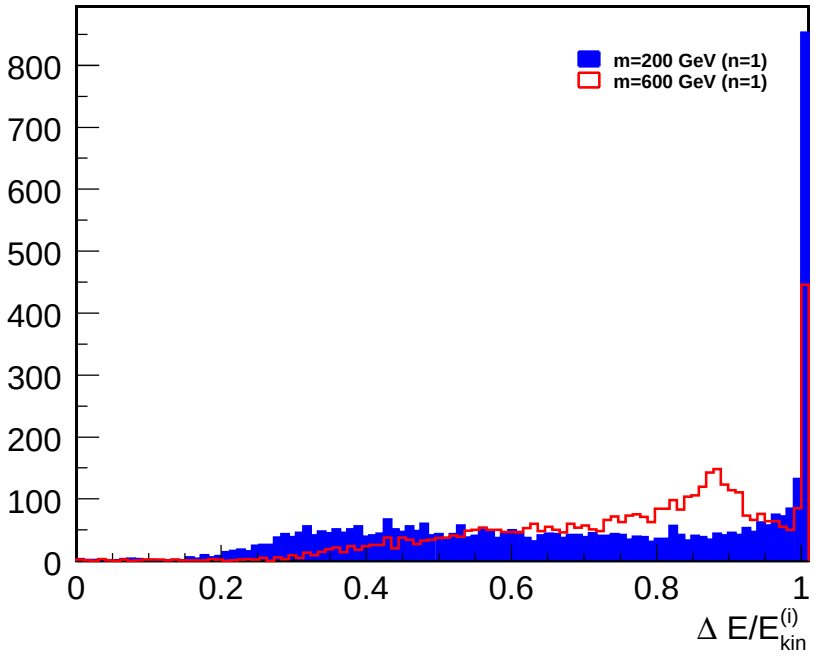

Figure 4.11: Relative energy loss of 200 GeV and 600 GeV monopoles in the COT end caps. The rate of magnetic charge which travels to the calorimetry placed in the CDF forward region is considerably lowered.

4.4 Time-of-Flight Acceptance

In order to project mass limits for the upcoming data taking periods of CDF, the acceptance of the TOF detector is computed for various projected masses. Magnetic charges featuring n=1,2 and 3 are taken into account where n is the quantum number in the Dirac Quantization Condition. A $m\overline{m}$ event is considered accepted if *one or both* monopoles reach a TOF scintillator. Masses between 200 GeV and 600 GeV are examined and about 5000 events are generated for each sample.

Figure 4.12 and Table 4.3 show the resulting acceptance versus projected monopole masses for different choices of the Dirac quantum number n. The magnetic field bends magnetic charge into the z direction and causes some particles to go outside of the acceptance of the Time-of-Flight detector. When studying the acceptance in dependence of the monopole mass, two effects have to be considered, which lower the acceptance at both ends of the considered mass spectrum. First, the larger the monopole mass, the smaller the bending, since the force is constant. Secondly, the momentum spectrum of monopoles of a certain assumed mass is limited by the center-of-mass energy of the colliding beam, about 2 TeV in case of the Tevatron. The kinetic energy of a monopole pair is determined by the difference between the total energy of the respective $q\overline{q}$ interaction and the di-monopole rest mass.

Moreover, the Time-of-Flight acceptance is affected by the choice of the integral number n in the DQC. Besides the increased bending, energy loss effects are magnified by a factor of n^2, making it more likely for magnetic charge to get stuck at low radii for $n > 1$.

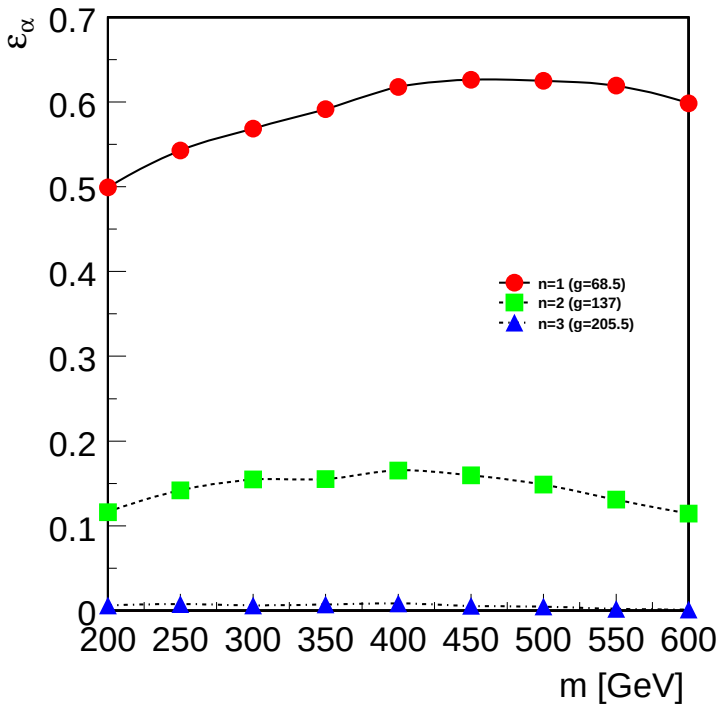

Figure 4.12: TOF acceptance ϵ_a for various projected monopole masses m and n=1,2,3

m [GeV]	$n=1$	$n=2$	$n=3$
200	0.499	0.116	0.0062
250	0.543	0.142	0.0077
300	0.569	0.155	0.0063
350	0.591	0.155	0.0072
400	0.618	0.165	0.0086
450	0.626	0.159	0.0056
500	0.625	0.149	0.0047
550	0.619	0.131	0.0021
600	0.599	0.114	0.0014

Table 4.3: Time-of-Flight acceptance ϵ_a

4.5 Mass Limits for the CDF RunII Data Taking Period

The production cross section calculated in Section 2.5.2 and Time-of-Flight acceptance simulated in Section 4.4 are combined with the projected integrated luminosities of Run IIa and Run IIb of the CDF Experiment, 2 fb^{-1} and 15 fb^{-1}, respectively, to determine the number of expected signal events N_{sig}. N_{sig} is calculated according to

$$N_{sig} = \mathcal{L} \cdot \sigma \cdot \epsilon_a$$

and thus Figure 4.13 and Figure 4.14 are derived. The obtained results are further documented in Table 4.4. A mass reach of 490 GeV for Run IIa and 560 GeV for Run IIb for is achieved for $n = 1$. This assumes 100 percent trigger efficiency and a single event discovery due to the unique signature of the monopole. Background has to be measured and studied once the Time-of-Flight system is ready to process collisions from the Tevatron in order to prove that this assumption is correct.

m [GeV]	$n = 1$		$n = 2$		$n = 3$	
200	5452.39	40892.9	5074.34	38057.5	604.888	4536.66
250	1303.13	9773.47	1362.69	10220.2	166.501	1248.76
300	322.178	2416.33	350.343	2627.57	31.943	239.572
350	78.5967	589.475	82.4668	618.501	8.65144	64.8858
400	18.3569	137.677	19.6664	147.498	2.29158	17.1869
450	4.1424	31.068	4.2187	31.6402	0.331119	2.48339
500	0.82412	6.18092	0.78439	5.8829	0.05610	0.42076
550	0.14558	1.09187	0.12302	0.92263	0.0045	0.03378
600	0.02086	0.15647	0.01596	0.11969	0.00043	0.00324

Table 4.4: Number of expected signal events for Run IIa and Run IIb

Figure 4.13 and Figure 4.14 suggest that the direct search with the Time-of-Flight system at CDF is equally sensitive to monopoles with $n = 1$ and $n = 2$. Note though, that a perturbative calculated cross section is scaled with a numerically large factor of $(ng/e)^2 \approx n^2$.

4692. It has already been stated that this method does not do any better than produce qualitative meaningful results for $n = 1$. The credibility further decreases for larger choices of the Dirac quantum number n. The uncertainty of the production cross section caused by the lack of a non-perturbative field description of the process just effects the quality of the presented mass reach projection. The presented search method, based on the highly ionizing signature and the unique parabola track of a magnetic charge are independent of the production theory and stand on a solid ground.

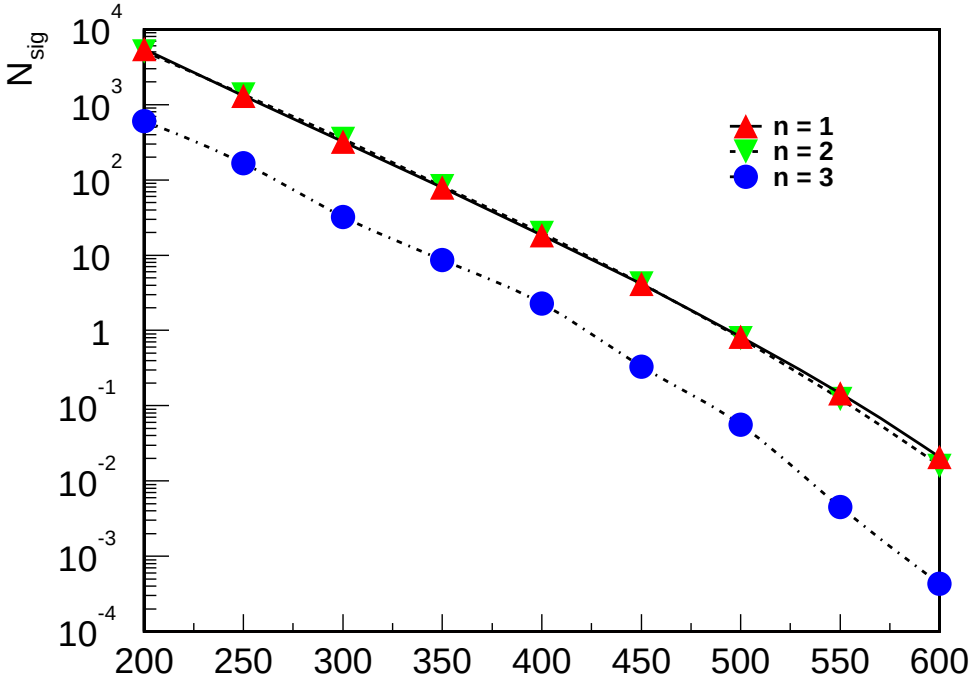

Figure 4.13: N_{sig} for Run IIa ($\mathcal{L}_a = 2$ fb^{-1})

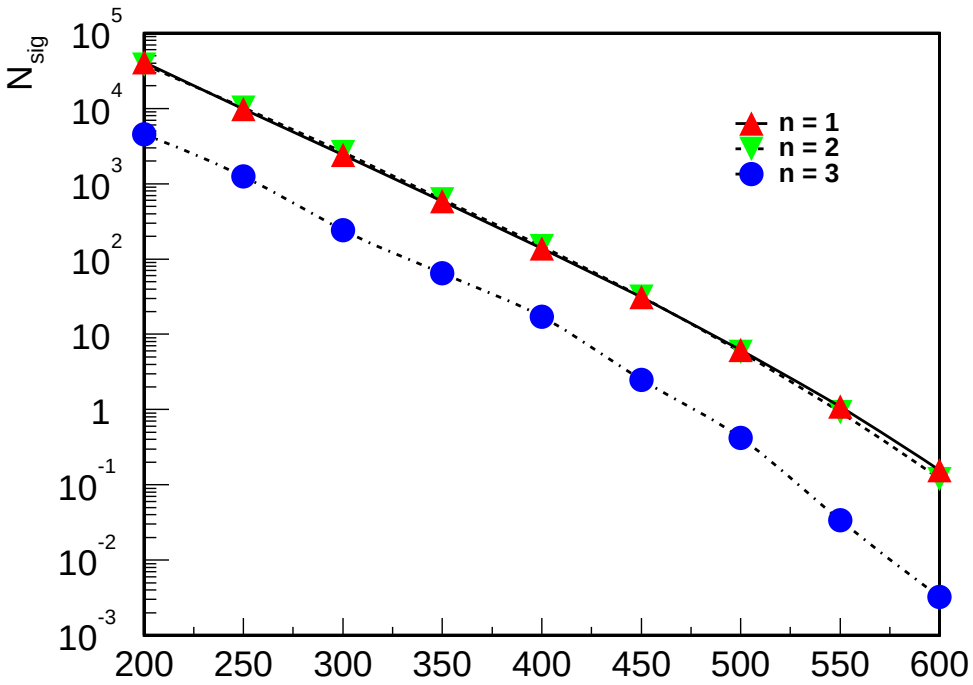

Figure 4.14: N_{sig} for Run IIb ($\mathcal{L}_b = 15$ fb^{-1})

4.6 Arrival Times at the Time-of-Flight detector

The time a monopole requires to reach the Time-of-Flight detector is potentially large, since monopoles are expected to be heavy. Because there is just a limited time window of about 50 ns to measure signals, it has to be investigated if this causes problems. Figure 4.15 shows flight time distributions for TOF accepted monopole events for masses of 200 GeV and 600 GeV. Besides the raw flight time from the production vertex to the scintillator hitpoint, the t0-smearing caused by the bunch length and the time the light needs to travel to *both* PMT's are taken into account. Figure 4.16 illustrates the discrepancies between raw flight time and the time when the signal reaches the electronics for a monopole mass of 600 GeV and $n = 1$. It is important to require coincidence at both ends of the TOF scintillator in order to obtain a meaningful measurement. Therefore, it is considered insufficient to just have the signal of the PMT closest to the hitpoint within the window. Still the flight times appear to be well behaved and covered in the required window even for 600 GeV monopoles.

Note that each bar measures only one signal per event; therefore, a slow particle could remain undetected and not cause the trigger, if it hits a scintillator bar that has already seen a faster particle in the same event. This effect is expected to be less than 10 percent which is the typical occupancy.

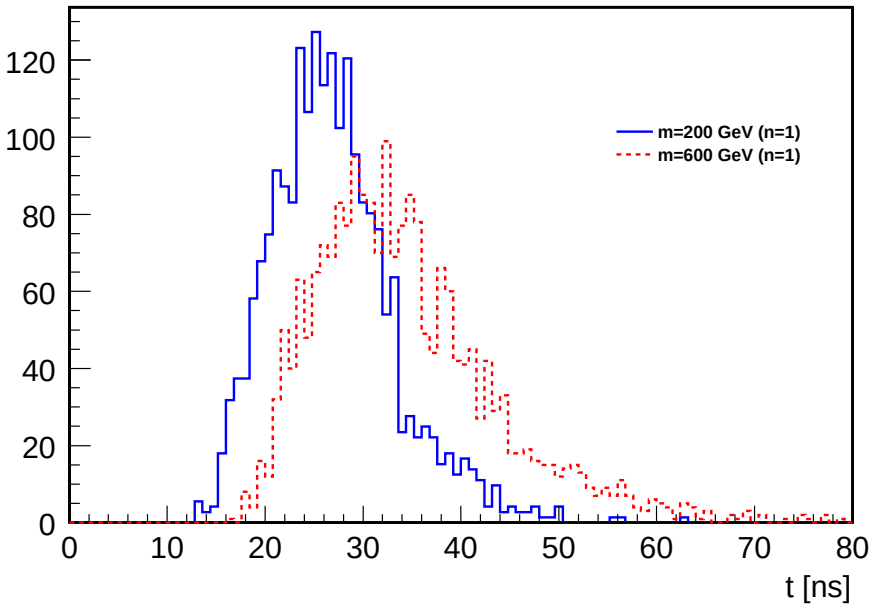

Figure 4.15: Flight time distributions for monopoles featuring m=200 GeV and m=600 GeV

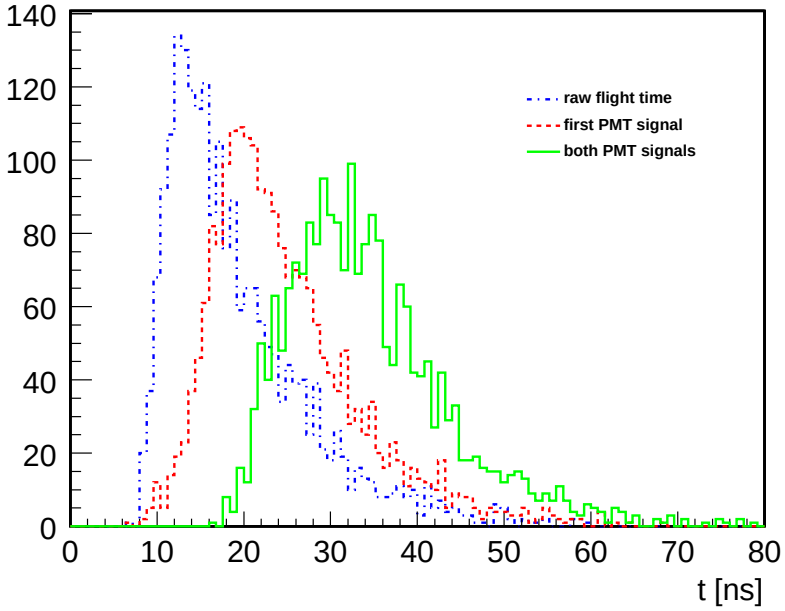

Figure 4.16: Discrepancies between raw flight time and signal arriving at PMT's for m=600 GeV

Chapter 5

GEANT Implementation and Simulation

5.1 Overview of the GEANT3 Tracking System

To simulate the passage of particles through matter as well as the electronic response of specified detector systems, high energy physicists commonly use a software package called GEANT [9]. "Tracking" a particle through some defined detector geometry refers to the integration of the equations of motion of the particle and thereby evaluating successive steps of the particle's trajectory. Additionally to the kinematics of the particle, which are usually determined by its charge, mass and the field configuration of the traversed space, each step has to feature corrections to account for the presence of matter. The different ways a particle interacts with the experimental setup are refered to as physical processes. Some of these processes are energy loss due to ionization, multiple scattering, δ-ray production, decay, energy loss due to bremsstrahlung or Cherenkov light production.

The critical task when tracking a particle through a complex detector structure is efficient step size determination, taking into account the processes named above as well as the geometry itself. The step length is limited by the path length to the next material boundary as well as by constraints set by the physical processes.

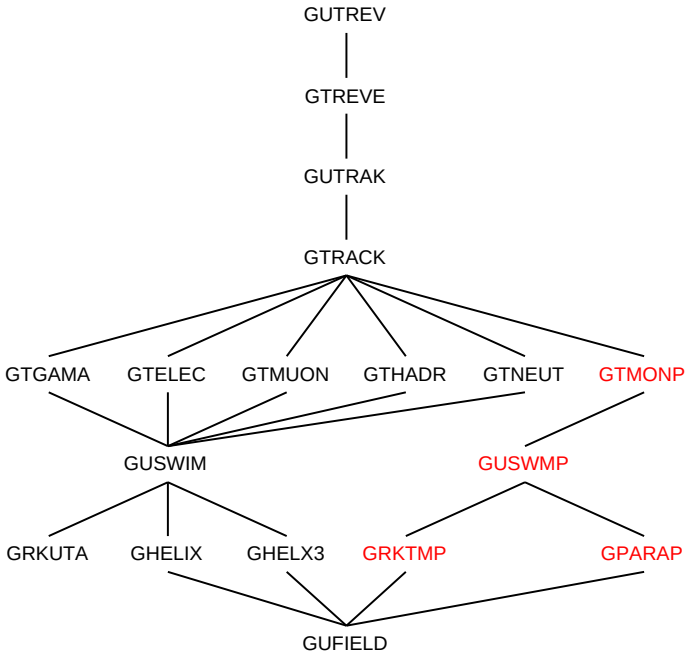

Figure 5.1: Structure of the GEANT tracking package

5.1.1 Structure of the GEANT3 Tracking Algorithm

The way particle tracking is implemented in GEANT 3 is illustrated in Figure 5.1. Routines which start with "`GU`" are usually empty by default and allow the user to implement code which is called at well defined entry points into the simulation process. The entry points can be used for various purposes like printing out debug information, specifying the tracking of secondary particles or handling the detector response of a self-implemented geometry.

The tracking at event level is controlled by `GTREVE` called by `GUTREV` where the user can perform additional action before/after each event is tracked. `GTREVE` loops over all particles in one event and initializes the track with its primary parameters before calling `GTRACK`. Parameters are for example the particle type, initial position, energy and momentum. It is called by the user routine `GUTRAK` to hand control to the user before each particle is tracked. `GTRACK` uses the position of the particle to figure out the current medium and loads its material parameters. The variable `ITRTYP` determines one of eight possible tracking types the particle is assigned to and each type has its corresponding tracking routine, called in every step by

ITRTYP	routine	particles (incomplete)
1	GTGAMA	γ
2	GTELEC	e^-, e^+
3	GTNEUT	neutrons
4	GTHADR	hadrons
5	GTMUON	μ^-, μ^+
6	GTNINO	geantino (debugging)
7	GTCKOV	cherenkov photons
8	GTHION	heavy ions

Table 5.1: GEANT tracking routines, called by GTRACK according to the particle's tracking type, ITRTYP

GTRACK. They are listed in Table 5.1, together with some examples of particles each type refers to.

5.1.2 Process Management

Before computing the next point, each tracking routine evaluates the maximum step length allowed by all active processes for the respective particle type. A process is considered active, if its underlying physics apply to the currently tracked particle. For example, "decay" is not an active process for stable particles; neither is "hadronic interaction" for leptons. GEANT distinguishes three types of processes:

- *continuous processes*, like energy loss due to ionization, multiple scattering
- *discrete processes*, like δ-ray production, decay
- *pseudo processes*, like boundary crossing, maximum energy loss fraction per step

The interaction length assigned to each process is computed before tracking a particle. The difference between the current path length and the interaction length is evaluated and updated

in each tracking step. A process can occur and is evaluated only at those trajectory points, where the path length equals an integer multiple of the interaction length of the process. This enhances the simulation speed considerably, since the number of interaction points for most processes is smaller than the number of total steps to be computed. For example, an unstable particle might have just been checked for decay and afterwards crossed a material boundary, traveling just fractions of 1 mm; it would be inefficient to check on the particle's decay again.

Some processes, like energy loss and multiple scattering, have to be evaluated in every step and have therefore not assigned an interaction length.

5.1.3 Step Size Determination and Swimming a Particle

Step Size

The distance between the current location and the next to be computed is defined as *step size*. Each active process constrains the step size and sets a maximum limit. For geometry constraints, the estimated distance to the next boundary is updated in each step and reevaluated by `GTNEXT` when necessary based on linear extrapolation. The minimum of all these maxima set by the different processes determines the current step size, which is passed to `GUSWIM`, if the particle is charged. Otherwise, the track gets linearly extrapolated, according to its current momentum.

Swimming the Particle through the Current Step

The routine `GUSWIM` manages the swimming of charged particles according to the field configuration defined in the detector geometry. The `IFIELD` flag provides information about the magnetic field present at the current space point. If the magnetic field is arbitrary (`IFIELD=1`), `GRKUTA` performs a fourth order Runge-Kutta integration in order to compute the next trajectory point. If the magnetic field is constant (`IFIELD=2`) or even has just one nonzero component in z-direction (`IFIELD=3`), the optimized routines `GHELIX` and `GHELX3` are used respectively to swim the particle. All three routines are constrained to provide the desired step size between the current and the newly computed location. Once the appropriate routine

is chosen, GUFIELD will be called, which is supposed to implement the magnetic field vector at every point of the experimental setup.

Applying Physical Processes

After the particle has been transported, all active processes are applied. The tracking routine calculates multiple scattering and energy loss, and updates the particle's kinematics; Discrete processes are evaluated if suggested by their interaction length and in case of occurrence, the final state is generated; Secondary particles are generated where appropriate and stored in a separate stack to be tracked later. This procedure repeats until the end of the particle trajectory, which is determined by one of the following four processes:

- *stop*: the particle lost all its kinetic energy through its interaction with matter.
- *decay*: the particle decayed into a final state of other particles. The final state is computed and the daughter particles are put into a stack to be tracked later.
- *interaction*: the particle interacts and the final state has to be generated. New particles are put into a stack to be tracked later.
- *escape*: the particle travels outside the boundaries of the experimental setup.

Figure 5.2 illustrates one step of the described tracking algorithm for the GTHADR routine.

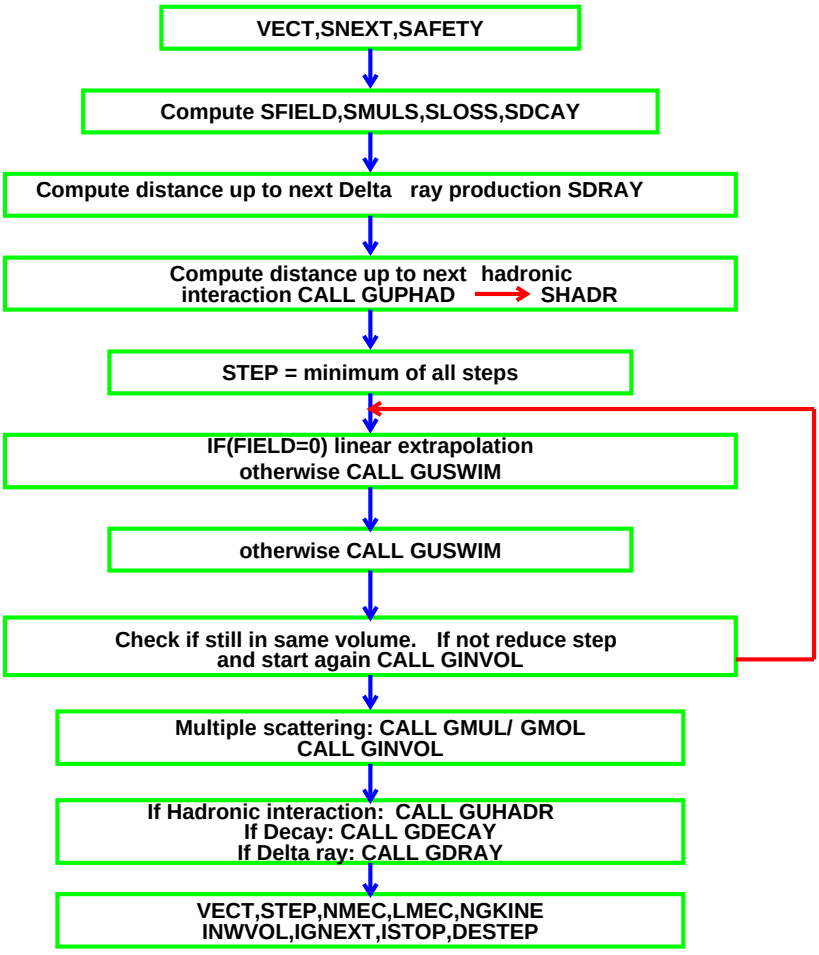

Figure 5.2: GTHADR: tracking hadrons in GEANT3 as a tracking routine example

5.2 Implementation of Monopole Tracking

5.2.1 Kinematics

The tracking package is extended to perform tracking of magnetic charge. Figure 5.1 depicts how the tracking algorithm is modified. A new tracking type, `ITRTYP = 9` is defined to label magnetic monopoles. The `CHARGE` variable, which is meant to store the *electric* charge of a particle, is used to store the magnetic charge of a monopole while the electric charge is assumed to be zero. The implementation does not support dyon[1] tracking and no routine has been implemented to deal with the kinematics of a particle carrying both electric and magnetic charge.

A new tracking routine, `GTMONP` is implemented to deal with particles of tracking type `ITRTYP=9`. It is called by `GTRACK` in the same fashion as the other tracking routines. Its structure is shown in Figure 5.3.

In order to transport a monopole according to the kinematics presented in Section 2.2, `GTMONP` calls a new routine, `GUSWMP` instead of `GUSWIM`. The routine `GUSWMP` checks on the active magnetic field configuration at the current location and calls the respective tracking routine. If the magnetic field is constant and along the z-axis, `GPARAB` calculates the step evaluating the analytical solution found in Section 2.2. The `GPARAB` routine uses a special algorithm to transform the given step size into the respective time interval. For an arbitrary magnetic field configuration, `GRKTMP` performs a fourth-order Runge-Kutta integration to compute the new position. The set of two first-order time-dependent differential equations to be solved,

$$\begin{aligned} \dot{\vec{p}} &= g \cdot \vec{B} \\ \dot{\vec{x}} &= \vec{p}/m \end{aligned}$$

is transformed into a representation based on the path length $s = \sqrt{x_1^2 + x_2^2 + x_3^2}$ through

$$\frac{d}{dt} = \frac{ds}{dt}\frac{d}{ds} = v \cdot \frac{d}{ds}$$

[1] A dyon is a particle which carries both electric and magnetic charge

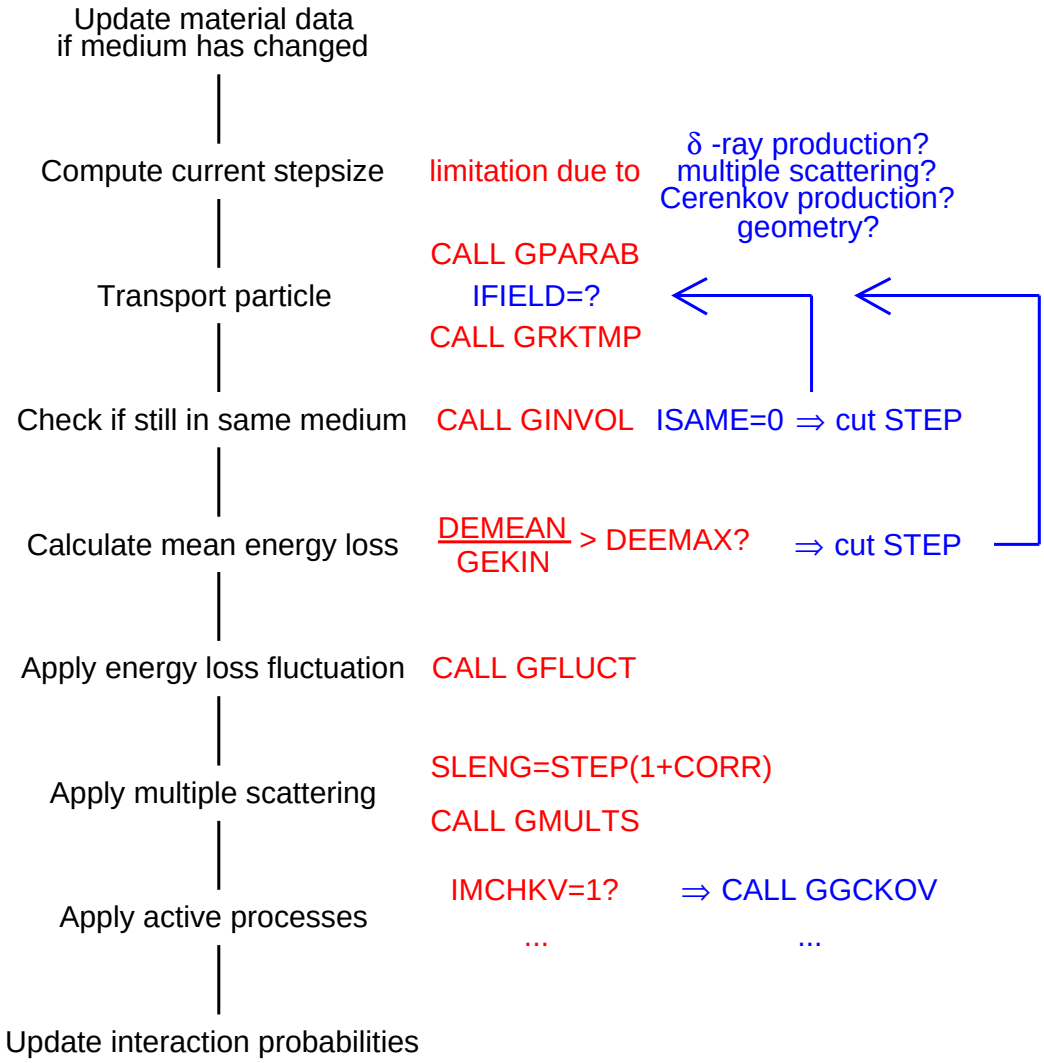

Figure 5.3: Structure of monopole tracking routine GTMONP

to

$$\begin{aligned} \frac{dp}{ds} &= \frac{g\vec{B}}{v} \\ \frac{dx}{ds} &= \vec{p}/p \end{aligned}$$

The set of equations is integrated over the current step size given by `GTMONP` according to the Runge-Kutta implementation presented in Reference [18]. The absolute error on the step size is estimated as a function of the particle momentum and delivers another constraint on the maximum stepsize. It is therefore evaluated in `GTMONP` before `GUSWMP` is called in case the field configuration demands Runge-Kutta integration.

5.2.2 Energy Loss

The Bethe-Bloch formula suggests, that the energy loss due to ionization does not depend on the particle mass but just on its $\beta\gamma$ for $m \gg m_e$. Therefore, GEANT computes tables for energy loss $\frac{dE}{dx}(E_{kin})$ and range $R(E_{kin})$ for all materials at the beginning of a simulation for three kinds of particles: electrons, muons, and protons or all other particles. Since monopoles are assumed to be heavy, the proton table is used to compute energy loss of a magnetic charge. The table features energy loss values for a spectrum of 90 kinetic energy values, which are stored in the array `ELOW`. The energy loss for a monopole of kinetic energy E_0 is calculated according to the following algorithm:

1. Calculate the kinetic energy T_0 of a proton with the same β like the monopole:

$$T_0 = \frac{m_p}{m_{mon}} \cdot T_{mon}$$

2. Determine interval in energy loss table which contains T_0 ($T_i \equiv ELOW(i)$):

$$T_i < T_0 \leq T_{i+i} \quad , i = 1, ..., 90$$

3. Compute energy loss through linear interpolation:

$$\frac{dE}{dx}(T_0) = \frac{dE}{dx}(T_i) + \frac{T_0 - T_i}{T_{i+1} - T_i} \cdot \left(\frac{dE}{dx}(T_{i+1}) - \frac{dE}{dx}(T_i) \right)$$

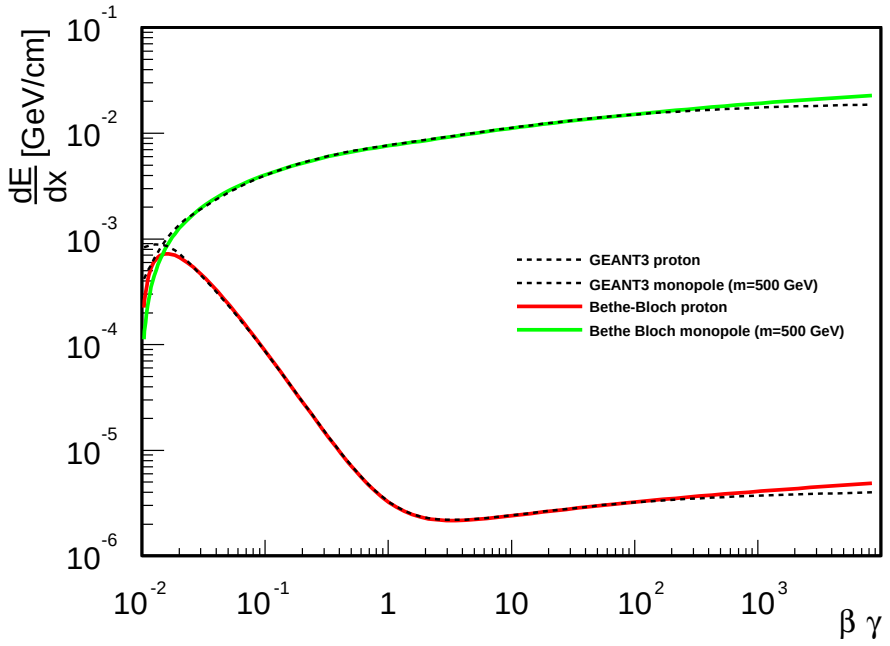

Figure 5.4: Energy Loss, calculated according to Bethe-Bloch and obtained from precalculated GEANT tables (medium:air)

4. modify result according to the monopole modification of Bethe Bloch presented in Equation (2.25):

$$\frac{dE}{dx}^{mon}(T_0) = \frac{dE}{dx}(T_0) \cdot g^2 \cdot \beta^2$$

Figure 5.4 compares the derived GEANT energy loss table for magnetic monopoles with Equation (2.31). The original GEANT proton loss curve is also depicted as well as the Bethe-Bloch energy loss of a proton[2]. The energy loss for a monopole in GEANT extracted from the proton table matches Equation (2.31) nicely. The curves diverge for $\beta\gamma < 2 \cdot 10^{-2}$. The Bethe-Bloch is valid only if the incident particle is faster than the orbital velocity of the atomic electrons. Therefore, the GEANT energy tables are parametrized based on fitted empirical data at low kinetic energies.

Since version 3.15, GEANT uses a variation of the algorithm to determine the energy loss of a particle. It is based on the *stopping range* of the particle which is tabulated using the

[2]Calculated according to Equation (2.22) with shell correction term $C_e = 0$ and density effect correction term $\delta = 0$

energy loss tables according to

$$R(E_0) = \int_{E_0}^{0} \frac{dx}{dE} dE \quad .$$

Therefore, the monopole stopping range is given by

$$R_{mon}(E_0) = \frac{1}{(ng)^2} \int_{T}^{0} \frac{1}{\beta\,(E)^2} \frac{dx}{dE} dE \quad .$$

Due to the dependence of β on the integration parameter E, the stopping range of a monopole cannot be obtained from the proton table but would require its own table. The advantage of the new algorithm, which moreover uses a quadratic interpolation, is a smaller error at low kinetic energies. The error of the linear approximation is $\mathcal{O}\left(\partial^2 E/\partial x \partial E_{kin}\right)$. Therefore, the energy loss is overestimated at low kinetic energies due to the $1/\beta^2$ term of the Bethe-Bloch equation. Since this term vanishes for magnetic charge, the linear interpolation leads to small overestimation as shown in Figure 5.4. Therefore, the old algorithm is used for magnetic charge thereby avoiding the need for an extra monopole table to be calculated for every material.

5.2.3 Energy Loss fluctuations

Due to the statistical nature of energy loss, large fluctuations occur from time to time. The description of these fluctuations is characterized by the *significance parameter* κ:

$$\kappa = \frac{\xi}{T_{max}}$$

with T_{max} the maximum transferable energy in a single collision with an atomic electron defined in Equation (2.23) and ξ the mean energy loss,

$$\xi = \frac{2\pi z^2 e^4 N_{Av} Z \rho \delta x}{m_e \beta^2 c^2 A} = 0.1534 \cdot 10^{-3} \frac{z^2}{\beta^2} \frac{Z}{A} \rho \delta x GeV$$

where δx is the thickness of the traversed material layer. The coefficient κ measures the contribution of collisions with energy transfer close to T_{max}. It tends towards large values for large δx and small β and vice versa. GEANT uses three different models involving three distributions to describe energy loss fluctuations in different regimes of κ:

- *Gaussian distribution* for $\kappa > 10$; a large number of collisions leads to the loss of most or all energy of the incident particle

- *Vavilov distribution* for $0.01 < \kappa < 10$
- *Landau distribution* for $\kappa < 0.01$

A detailed discussion of all three models is given in Reference [9]. The only modification for fluctuations of magnetic charge consists of the replacement $z \cdot e \rightarrow n \cdot \beta \cdot g$ in the mean energy loss:

$$\xi_{mon} = 0.1534 \cdot 10^{-3} \frac{(ng)^2}{e^2} \frac{Z}{A} \rho \delta x GeV$$

The resulting κ_{mon} leads to the correct treatment of magnetic monopoles by the fluctuation models already implemented in GEANT.

5.2.4 Multiple Scattering

To simulate multiple scattering effects, GEANT implements two different models: Molière scattering and the Gaussian multiple scattering approximation. Since scattering angles are typically small for magnetic charge, the multiple scattering of a magnetic monopole is treated using the Gaussian model. The width of the angular distribution for charged particles is calculated differently from Equation (2.24) as

$$\theta_0 = 2.557 \chi_{cc} \frac{\sqrt{x}}{E\beta^2}$$

where χ_{cc} is a parameter from the Moliere theory, that depends linearly on the charge of the incident particle. A detailed description of the Molière theory is given in Reference [9].

The monopole modification $z \cdot e \rightarrow n \cdot \beta \cdot g$ leads to

$$\theta_0 = 2.557 \chi_{cc} \frac{\sqrt{x}}{E\beta} = 2.557 \chi_{cc} \frac{\sqrt{x}}{pc}$$

The Gaussian model is implemented in the GEANT routine `GMGAUS`, which is called with β as a parameter instead of β^2 for magnetic charge.

5.3 Comparison with stand-alone Simulation

In order to validate the monopole tracking implemented in GEANT3, a cross check with the stand alone simulation is performed. The same sample of 552 $m\bar{m}$ events containing 500 GeV

monopoles (n=1) is tracked in both frameworks. For all particles, which are accepted by the Time-of-Flight detector according to the Simulation, it is checked if it also reaches the scintillator in GEANT. If it does, both positions of the TOF hitpoints are recorded and the absolute difference serves as a measure of agreement. Furthermore, the energies of the particles at the hitpoint are compared. This allows to compare the amount of material to be traversed in both applications.

Note that the geometry used in GEANT describes the CDF detector more accurate and in greater detail than the stand-alone simulation. The later assumes most subdetectors to be one part of cylindrical shape, where the GEANT geometry arranges more complex shapes like bars in a cylinder. Some detector parts, like the read out electronics of the SVX II, cooling pipes, and certain support structures, are not considered in the stand-alone program. Furthermore, the stand-alone simulation does not account for energy loss fluctuations.

The stand-alone tracking produces 432 TOF-accepted monopoles, 403 of which are as well TOF hits if tracked with GEANT. The Simulation and GEANT compute a TOF acceptance ϵ_a of 0.6069 and 0.6014, respectively, where there is a total of 438 particles accepted using GEANT. Figure 5.5 shows the absolute displacement of the TOF hitpoints of particles which are accepted by the TOF detector in both frameworks. Figure 5.6 and Figure 5.7 illustrate, that all displacement is due to the z coordinate. This makes sense since the parabolic shape of the monopole track in the longitudinal plain depends on the energy and therefore on the energy loss determined by the geometry, whereas the straight course in the transverse plane is not much affected in both systems. The asymmetry in Figure 5.7 is due to the Time-of-Flight bar description of GEANT, which implements them as real bars with square cross section, all of them cylindrically arranged. The stand-alone program treats the Time-of-Flight system as one cylinder. Figure 5.8 shows the difference between the energy spectra at the Time-of-Flight scintillator entry points. The discrepancies are due to the different geometries and energy loss fluctuation effects in GEANT.

The results are satisfactory and show, that monopole tracking is successfully implemented in GEANT. The tail in the absolute-displacement distribution Figure 5.5 is due to the large energy loss of magnetic charge. A single piece of matter can therefore make a huge difference,

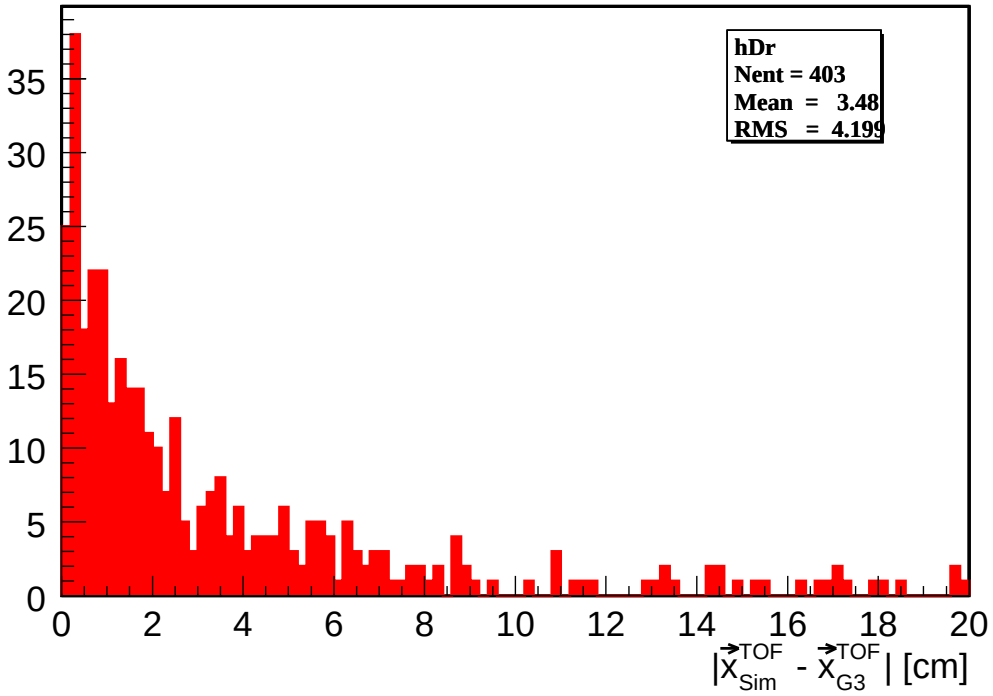

Figure 5.5: absolute displacement at TOF hitpoint

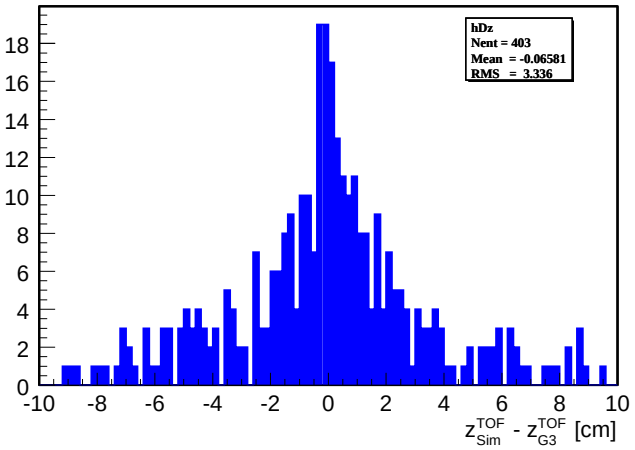

Figure 5.6: z-displacement at TOF hitpoint

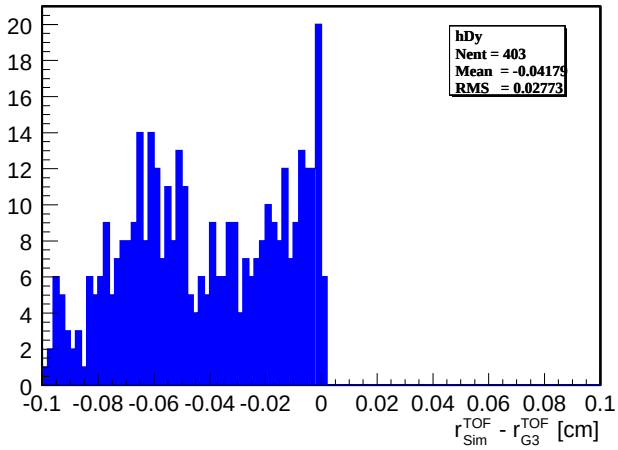

Figure 5.7: r-displacement at TOF hitpoint

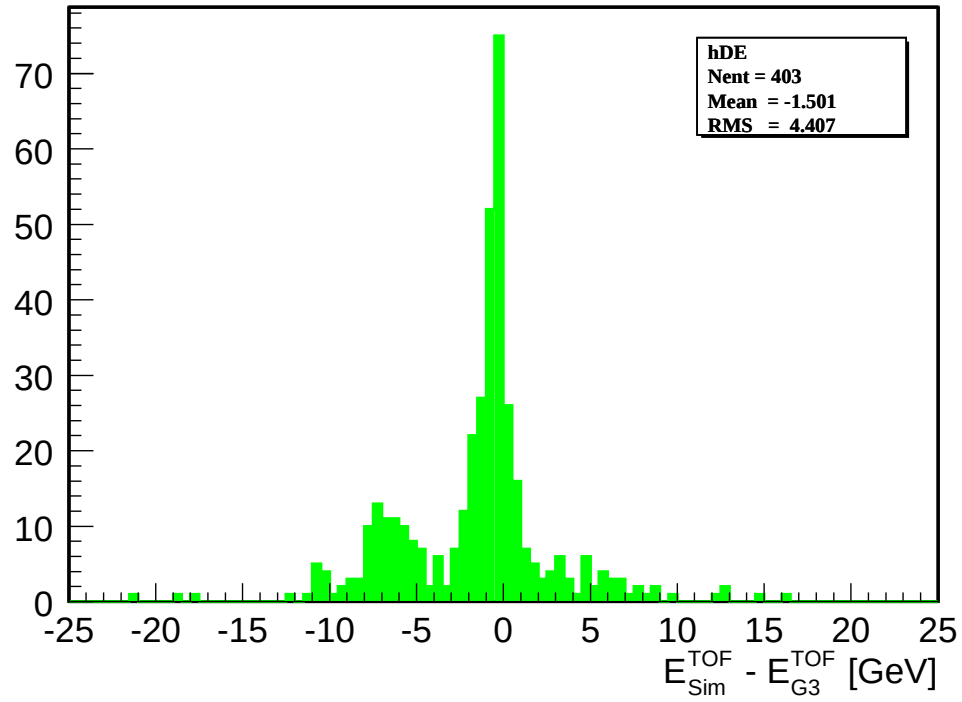

Figure 5.8: total energy difference at TOF hitpoint

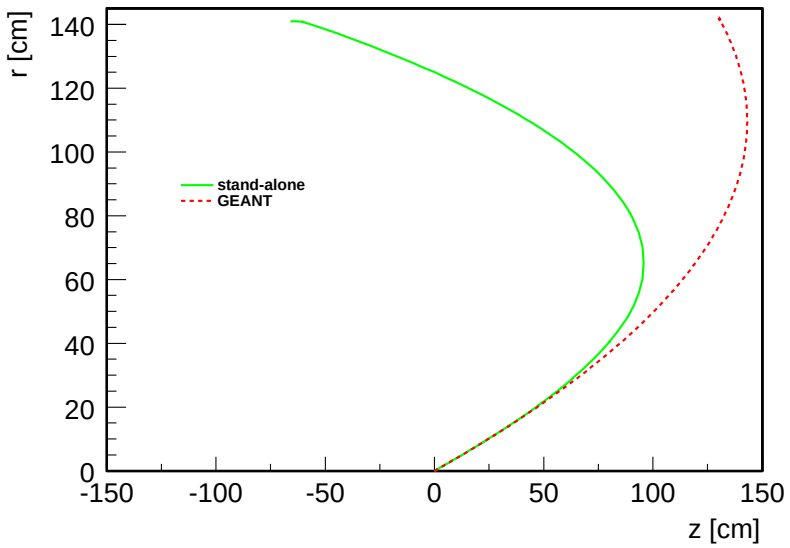

Figure 5.9: Trajectories of two monopoles with same initial kinematics but large TOF hitpoint displacement of 189.0 cm.

when it is traversed by the one but not the other particle. This effect is maximal, when the initial transversal momentum is anti-parallel to the direction, in which the magnetic field bends the particle. The turning point of the trajectory with respect to the beam axis is then different and the two compared particles travel in opposite direction. The effect is illustrated in Figure 5.9, where the track of two identically generated monopoles, which are displaced by 189.0 cm when hitting the Time-of-Flight detector, are shown in a two-dimensional projection. The energy of the two particles is shown in Figure 5.10. The magnetic charge tracked in the stand-alone program experiences a large loss of energy when traversing the ISL Hybrid electronics at $r \approx 14.0\ cm$. The monopole misses this part of the CDF detector when tracked with GEANT. Its turning point is at a larger radius and the stand-alone particle travels in opposite direction after turning, picking up more energy with its longitudinal momentum parallel to the magnetic force.

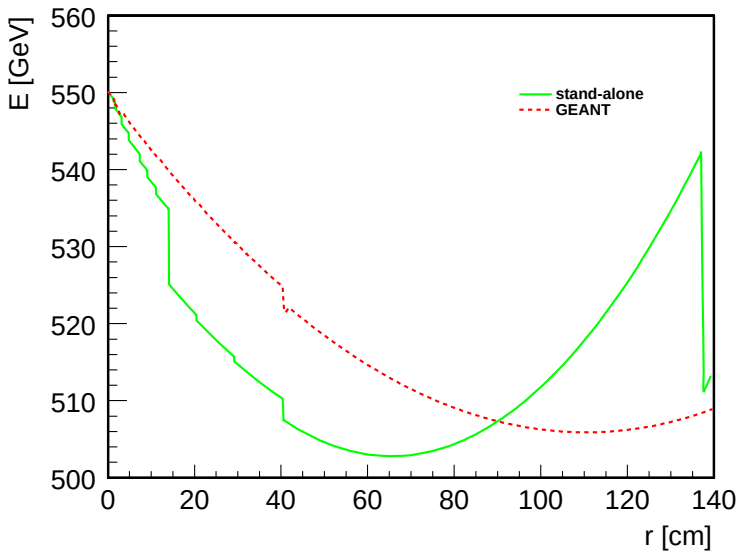

Figure 5.10: Energy of the two monopoles shown in Figure 5.9. The large energy loss of the particle tracked with the stand-alone program in the ISL hybrid leads to the large discrepancy at the TOF hitpoint. The large energy loss at 138.0 cm is due to the outer COT containment made of aluminum, which is not yet implemented in the GEANT CDF detector description.

Chapter 6

The Highly Ionizing Particle (HIP) Trigger

The Time-of-Flight[17] detector is sensitive to the highly ionizing signature of magnetic charge. A monopole trigger will be implemented at Level-1 triggering on large pulses. Figure 6.1 shows the structure of the Time-of-Flight system. In order to understand the trigger, the TOF signal path and read-out electronics are briefly described[19].

6.1 Signal Path

Each scintillator is read out at both ends by a photomultiplier tube (PMT).

A photomultiplier tube is a device which converts light into a measurable electric current. It consists of a cathode made of photosensitive material followed by a dynode string and finally an anode. An incident photon causes the cathode to emit an electron through the photoelectric effect. The high voltage applied to the tube directs the electron to the first dynode, where secondary electrons are produced upon striking. The electrons are further accelerated through the whole string of dynodes, until the thus created cascade is finally collected by the anode to give a current.

The photomultipliers used with the Time-of-Flight system are nineteen-stage finemesh tubes, which provide sufficient gain to be operated in the 1.4 T magnetic field of the CDF

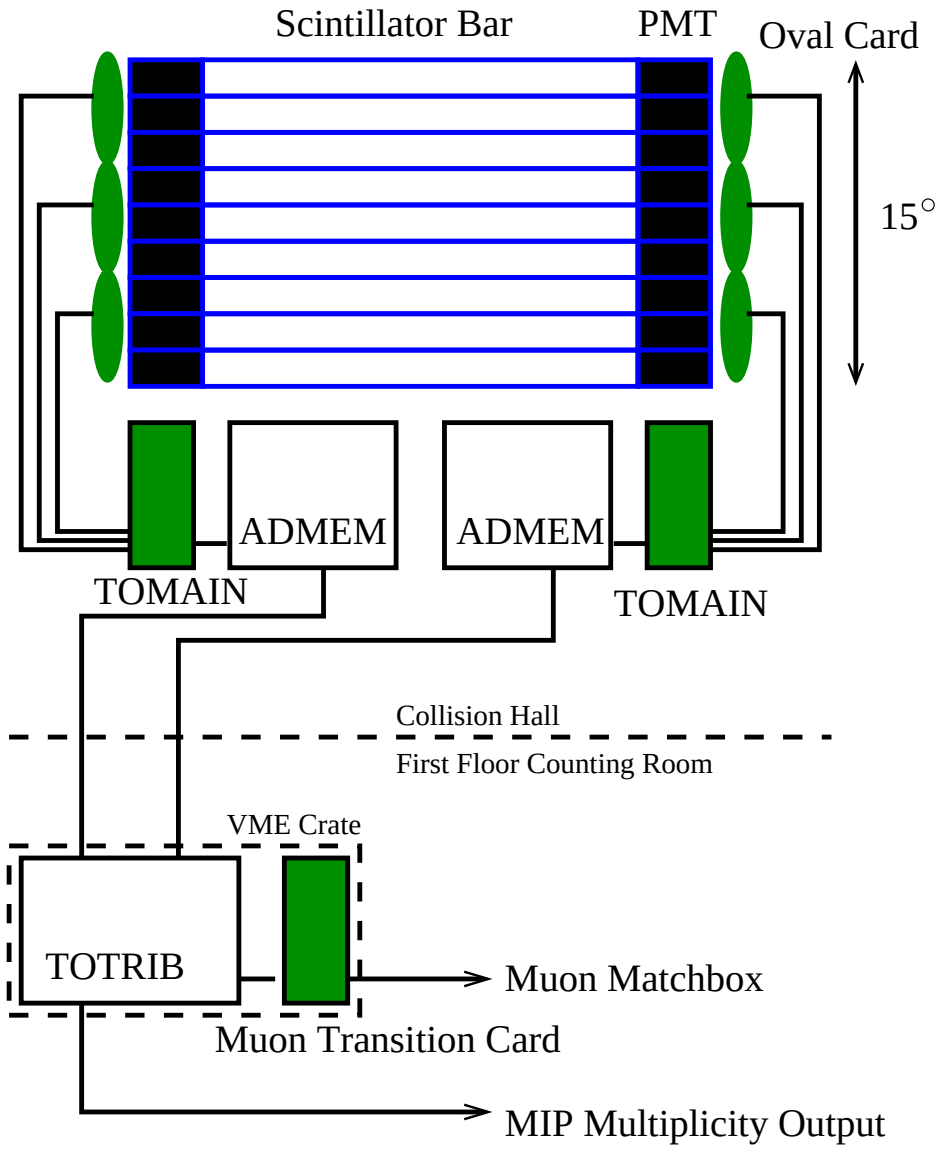

Figure 6.1: Organization of the Time-of-Flight read-out electronics

tracking system. The signal measured is formed by the difference between the pulse on the anode and the last dynode of the phototube. This ensures a sufficiently large signal and reduces signal noise through common mode rejection. For each PMT, the pulse arrival time and charge are measured. The PMT's are connected to the *phototube base*, a custom design circular printed circuit board which connects with the preamplifier. The phototube signal is on average reduced by a factor of 500 in amplitude by the1.4 T magnetic field. Since the PMT signal has a high source impedance and is asymmetrical, the preamplifier redrives it across 12 m of twisted pair cable as a differential signal with low source impedance suitable for transmission to the analog-to-digital conversion cards. The scintillator bars are organized in triplets, and each three-pack is terminated with an oval *connector board* that connects the high-voltage supply for the PMT's, the low-voltage for the preamplifiers and the twisted-pair signal cable.

The readout of hit time and charge of the phototube signal is performed using ADMEM modules, which are used and designed to measure the CDF calorimeter signal. To use these boards for the Time-of-Flight system, additional electronics are required which are located on the TOMAIN transition boards and process the signals before the ADMEM. 18 of the 20 channels available on the ADMEM are used to digitize TOF signals, that is 9 time and 9 charge measurements per board. The charge measurement is performed by daughter CAFE cards, which are normally installed on an ADMEM board to deal with the calorimeter signal. The Time-of-Flight detector is asked to deliver a timing precision of 25 ps, which can not be provided using the CAFE board with its 10-bit ADC. Therefore, a new board has been designed, containing a 12-bit ADC, which matches the precision needs for the timing measurement. Since the board is simpler in its design, it is refered to as the deCAF card.

6.2 Electronics

The phototube signal from the 12 m twisted-pair signal cable is received and after some signal shaping is split between a discriminator and a circuit used to measure charge. The discriminator output produces a start signal for timing, and a common stop signal is provided

by a special TOF clock fanout system for every event. The output of the discriminator also generates a gate that restricts the integration of the pulse, allowing only the pulse that fired the discriminator to be integrated. This prevents subsequent hits from other particles being included in the charge estimate. Therefore, each scintillator bar is sensitive only to one particle per bunch crossing. The time is measured by a time-to-amplitude converter (TAC), that produces a voltage proportional to the time between start and stop pulses.

In order to achieve the desired time resolution, the charge of each pulse is measured to account for *time walk corrections*. Since the discriminator threshold is set to some constant value, the time measurement will depend on the amplitude of the pulse due to its shape. Figure 6.2 illustrates the problem by showing two pulses of two different amplitudes. Although both particles responsible for these pulses reach the Time-of-Flight detector at the same time, the pulse with the higher amplitude will trigger the discriminator earlier. The time walk correction algorithm makes use of the charge measurement to compute a correction Δt. Note that if the described effect would not arise, it would not be necessary for the Time-of-Flight detector to perform a charge measurement and the monopole trigger could not be implemented.

6.3 Trigger Logic

The Highly Ionizing Particle (HIP) Trigger[20] requires coincident signals from both ends of one scintillator bar to pass the heavy ionizing threshold, which is individually set for each channel. The digitized time and charge measurements are put in the Level-1 pipeline and sent through the programmable ADMEM Xilinx chip. Figure 6.3 depicts the strategy of the chip logic for two adjacent scintillator bars. The time measurement is not considered other than having to be in the events time gate. The charge measurement has to pass a discriminator which is set to the highly ionizing threshold of the respective channel. Without significant loss in efficiency or increase in rate, two adjacent channels are joined by a logical OR. The produced HIP bit is send out to the Time-of-Flight trigger board, TOTRIB. The trigger decision for each pair of bars is made by the TOTRIB based on the respective HIP bits from the east and west side of the detector, connected through a logical AND to assure coincidence. A positive

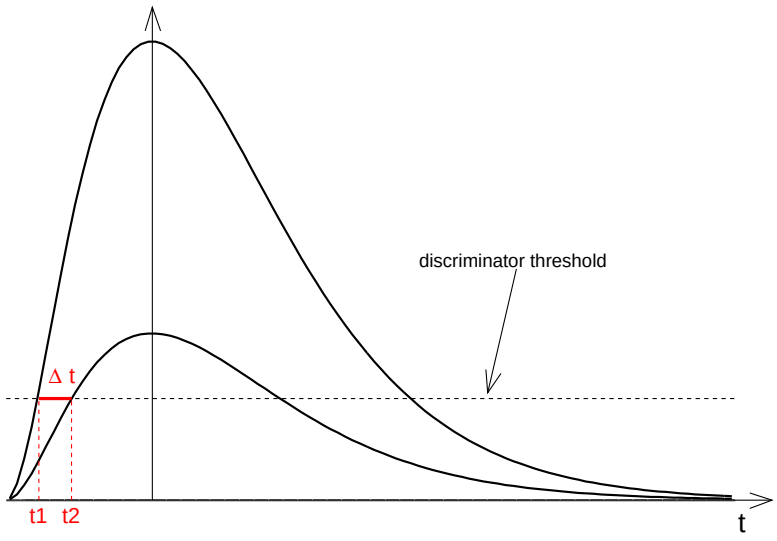

Figure 6.2: Two pulses of two particles arriving at the Time-of-Flight detector at the same time. The different pulse height leads to different time measurements, which are accounted for by time-walk corrections. These make use of the integrated charge measurement. They are essential since the typical rise time of a signal pulse is several ns, whereas the desired resolution of the time measurement is about 25 ps.

trigger decision requires just one HIP hit in the whole system.

Additionally, a multiplicity trigger is implemented as part of the TOF trigger requiring a minimum number of standard minimum ionizing hits (MIP), which will not be discussed here.

Within the overall CDF triggering scheme, this trigger is designed to contribute with about one percent to the overall rate. To control the rates, thresholds are tunable through the programmable Xilinx chip on the ADMEM. Moreover, hits can be correlated to tracks in the XFT by the TOTRIB board to significantly reduce noise.

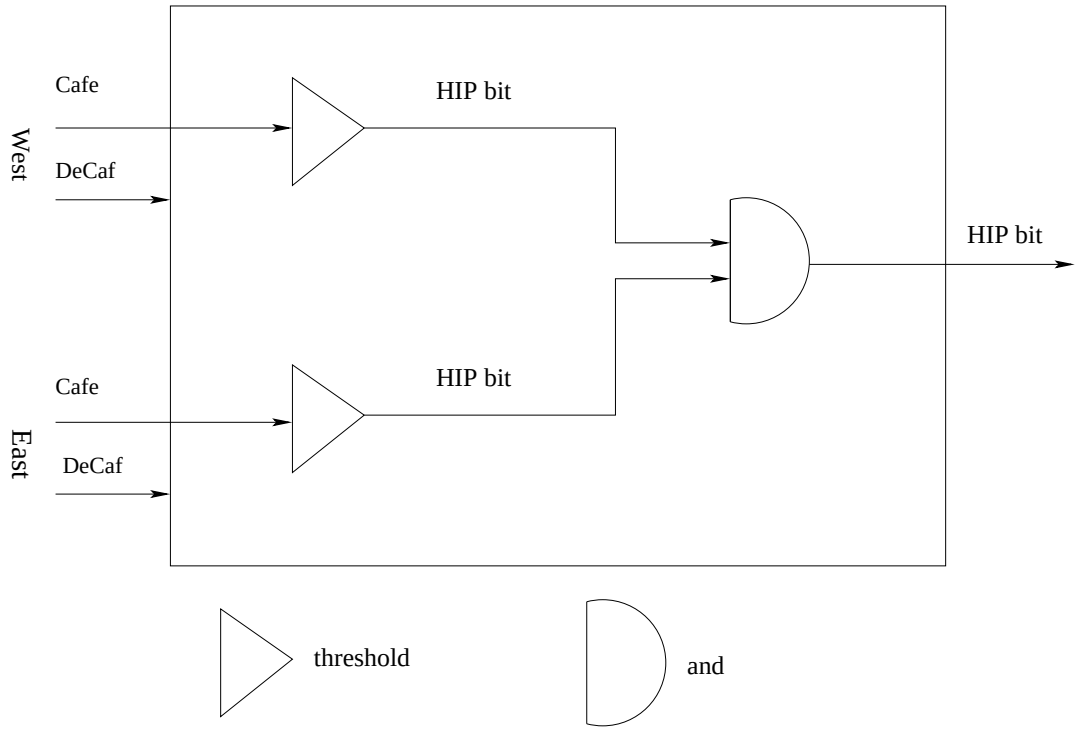

Figure 6.3: Trigger strategy for the Highly Ionizing Particle trigger. The charge measurements from both ends of a scintillator bar are combined to take the trigger decision. The time measurement is not considered.

Chapter 7

Outlook

The implementation of magnetic charge in GEANT and thereby in the CDF software framework offers a variety of possibilities to study the detector response of magnetic monopoles in CDF. The newly installed Time-of-Flight detector has been proven to be a suitable tool to trigger on the highly ionizing signature of magnetic charge candidates. It is not capable of a monopole discovery, since the highly ionizing signature is insufficient. A single event discovery requires the reconstruction of the monopole track using one or more subsystems provided by the integrated tracking system of CDF, mainly the COT drift chamber. The capability of generating monopole Monte Carlo within the CDF software framework will help developing offline pattern recognition algorithms to reconstruct the unique parabolic track. It will furthermore enable to tune trigger thresholds once a realistic simulation of Time-of-Flight electronics is implemented.

The projected monopole mass limits for the upcoming CDF data taking period, 490 GeV for Run IIa and 560 GeV for Run IIb, depend on the theoretical model of production. The Drell Yan production mechanism proposed is derived substituting electric by magnetic charges in the production cross-sections as suggested by the symmetrized Maxwell equations. The calculation of the latter, however, relies on perturbation theory which is only valid in the limit of small couplings. New approaches based on a non-perturbative dual QED treatment are under development. When these calculations become available the studies presented should be repeated to obtain more reliable monopole mass-limits.

SOME GREAT LAST SENTENCE

Bibliography

[1] P.A.M. Dirac, *Quantized Singularities In The Electromagnetic Field*, Proc. R. Soc. (London) A133, (1931).

[2] M. Ambrosio et al., *Magnetic Monopole Search With The Macro Detector At Gran Sasso*, INFN-AE-97-19, (1997).

[3] B. Abbot et al., *A Search for Heavy Pointlike Dirac Monopoles*, Fermilab-Pub-9 8/095-E, (1998).

[4] M. Acciarri et al., *Search For Anomalous $Z \to \gamma\gamma\gamma$ Events At Lep*, Phys. Lett. B345, (1995).

[5] L. Gamberg, G.R. Kalbfleisch, K.A. Milton, *Direct and Indirect Searches for Low-Mass Magnetic Monopoles*, hep-ph/9906526, (1999).

[6] L. Gamberg, K.A. Milton, *Dual quantum electrodynamics: Dyon-dyon and charge-monopole scattering in a high-energy approximation*, Phys. Rev. D 61, (2000).

[7] L. Gamberg, K.A. Milton, *Eikonal scattering of monopoles and dyons in dual QED*, OKHEP-00-05, (2000).

[8] G.R. Kalbfleisch, K.A. Milton, M.G. Strauss, L. Gamberg, E.H.Smith, and W. Luo, *Improved Experimental Limits on the Production of Magnetic Monopoles*, Phys. Rev. Lett. 85, (2000).

[9] *GEANT Detector Description and Simulation Tool*, CERN Program Library Writeup W5013, (1994).

[10] Torbjoern Sjoestrand, *Pythia 5.7 and Jetset 7.4 Physics and Manual*, (1998).

[11] J.D. Jackson, *Classical Electrodynamics*, Second Edition. New York: de Gruyter, (1982).

[12] J. Schwinger, L.L. DeRaad Jr., K.A. Milton, W. Tsai, *Classical Electrodynamics*, Reading, MA: Perseus Books, (1998).

[13] M.E. Peskin, D.V. Schroeder, *An Introduction to Qunatum Field Theory*, Reading, MA: Perseus Books, (1995).

[14] W. Greiner, J. Rafelski, *Spezielle Relativitätstheorie*, 3. überarb. Auflage. Frankfurt: Harri Deutsch, (1992).

[15] Particle Data Group, Eur. Phys. J. C3, 144 (1998).

[16] CDF Run II Technical Design Report.
On the WEB under: `http://www-cdf.fnal.gov/upgrades/tdr/tdr.html`

[17] The CDF Collaboration, *Proposal for Enhancement of the CDF II Detector with An Inner Silicon Layer and A Time of Flight Detector*, CDF Note 5096, (1998);
Update to Proposal P-909: Physics Performance of the CDF II Detector with An Inner Silicon Layer and A Time of Flight Detector, CDF Note 5264, (1999).

[18] W.H. Press, B.P. Flannery, S.A. Teukolsky, W.T. Vetterling, *Numerical Recipes in Pascal*, Cambridge University Press, (1989).

[19] C. Chen, M.Jones, J. Kroll, M.N. Newcomer, D. Usynin, R. Van Berg, *Electronics for the CDF TIme-of-Flight Detector: a Status Report*, CDF Note 5361, (2000).

[20] G. Bauer, M. Mulhearn, C. Paus, P. Schieferdecker,J. Konigsberg, J. Lewis, M. Albrow, N. Moggi, *Proposal of a Level-1 Trigger using the Time-ofFlight Detector*, CDF Note 5597, (2001).